ARMY RESEARCH LABORATORY

Modeling Nonlinear Elastic-plastic Behavior of RDX Single Crystals During Indentation

by John D. Clayton and Richard C. Becker

ARL-TR-5864 January 2012

NOTICES

Disclaimers

The findings in this report are not to be construed as an official Department of the Army position unless so designated by other authorized documents.

Citation of manufacturer's or trade names does not constitute an official endorsement or approval of the use thereof.

Destroy this report when it is no longer needed. Do not return it to the originator.

Army Research Laboratory

Aberdeen Proving Ground, MD 21005-5066

ARL-TR-5864 **January 2012**

Modeling Nonlinear Elastic-plastic Behavior of RDX Single Crystals During Indentation

John D. Clayton and Richard C. Becker

Weapons and Materials Research Directorate, ARL

REPORT DOCUMENTATION PAGE

Form Approved
OMB No. 0704-0188

1. REPORT DATE *(DD-MM-YYYY)*	2. REPORT TYPE	3. DATES COVERED (From - To)
January 2012	Final	October 2010-January 2012

4. TITLE AND SUBTITLE
Modeling Nonlinear Elastic-plastic Behavior of RDX Single Crystals During Indentation

5a. CONTRACT NUMBER

5b. GRANT NUMBER

5c. PROGRAM ELEMENT NUMBER

6. AUTHOR(S)
John D. Clayton
Richard C. Becker

5d. PROJECT NUMBER
AH80

5e. TASK NUMBER

5f. WORK UNIT NUMBER

7. PERFORMING ORGANIZATION NAME(S) AND ADDRESS(ES)
U.S. Army Research Laboratory
ATTN: RDRL-WMP-B
Aberdeen Proving Ground, MD 21005-5066

8. PERFORMING ORGANIZATION REPORT NUMBER
ARL-TR-5864

9. SPONSORING/MONITORING AGENCY NAME(S) AND ADDRESS(ES)

10. SPONSOR/MONITOR'S ACRONYM(S)

11. SPONSOR/MONITOR'S REPORT NUMBER(S)

12. DISTRIBUTION/AVAILABILITY STATEMENT
Approved for public release; distribution is unlimited.

13. SUPPLEMENTARY NOTES
Author email: <john.d.clayton1.civ@mail.mil>

14. ABSTRACT
A nonlinear anisotropic elastic-plastic model is developed for single crystals of the energetic material cyclotrimethylene trinitramine (RDX). The model accounts for orthorhombic symmetry of elastic constants, pressure-dependent compressibility, and dislocation glide on six slip systems. Numerical simulations of spherical indentation on oriented single crystals are performed. Model predictions are compared with experimental data and observations from the literature. Results demonstrate significant influences of elastic anisotropy and elastic nonlinearity. Model predictions for elastic response using elastic constants obtained from resonant ultrasound spectroscopy agree with experimental data; predicted forces obtained using constants obtained from Brillouin scattering tend to exceed experimental data. Predicted slip system activity is compared with that deduced from experimental observations of residual surface profiles. Indentation forces predicted by the nonlinear anisotropic elastic-perfectly plastic slip model exceed those observed in experiments, suggesting that surface and possibly subsurface fractures may contribute to a loss of stiffness in experiments at larger indentation depths.

15. SUBJECT TERMS
energetic material, molecular crystal, RDX, anisotropic elasticity, crystal plasticity, indentation

16. SECURITY CLASSIFICATION OF:			17. LIMITATION OF ABSTRACT	18. NUMBER OF PAGES	19a. NAME OF RESPONSIBLE PERSON
a. REPORT	b. ABSTRACT	c. THIS PAGE			John D. Clayton
Unclassified	Unclassified	Unclassified	UL	64	19b. TELEPHONE NUMBER (*Include area code*) 410-278-6146

Standard Form 298 (Rev. 8/98)
Prescribed by ANSI Std. Z39.18

Contents

List of Figures

List of Tables

Acknowledgment

D. E. Hooks and K. J. Ramos of Los Alamos are acknowledged for helpful suggestions.

INTENTIONALLY LEFT BLANK.

1. Introduction

Energetic molecular crystals are found in military and industrial applications involving explosives and propellants. For example, plastically bonded explosives consist of energetic crystals embedded in a waxy binder phase (*4*). Defects in energetic materials are thought to affect their initiation sensitivity. Local stresses may concentrate in the vicinity of cracks, pores, or lattice defects, including dislocations and point defects, which may, in turn, affect initiation of reactions associated with burning or detonation (*5*). In anisotropic single crystals, availability of slip systems associated with glissile dislocations may lower peak stresses and decrease sensitivity to shock initiation (*6*).

The focus of this work is the mechanical behavior of the energetic material cyclotrimethylene trinitramine ($C_3H_6N_6O_6$), referred to as RDX (Research Development Explosive). Single crystals of RDX belong to an orthorhombic space group with eight molecules per unit cell. Dislocations in RDX have been characterized using etch pit (*7*) and x-ray topographic (*8, 9*) techniques. Likely slip systems for dislocation glide in RDX have been suggested by analysis of anisotropic hardness profiles (*10*) and indentation experiments (*3, 11*). The latter experiments (*3, 11*) also provide an estimate of the critical resolved shear stress associated with slip initiation, thought to be on the order of the theoretical strength (i.e., $\approx G/10 - G/20$, with G a representative elastic shear modulus), which corresponds physically to homogeneous dislocation nucleation. Inelastic behavior of RDX single crystals has also been probed using shock experiments (*6, 12*) and molecular dynamics simulations (*12–14*). RDX undergoes a polymorphic phase transition ($\alpha \rightarrow \gamma$) at pressures on the order of 4 GPa (*15, 16*); this phase transformation has also been studied using atomic models (*17, 18*).

Continuum crystal plasticity theory permits predictive mesoscale modeling of materials behavior at length scales larger than feasible using atomic or molecular models, but with greater resolution than that afforded by macroscopic elastic-plastic models that omit description of anisotropy and slip system activity. Grain interactions can be studied in direct numerical simulations via finite element models, wherein each crystal of a polycrystal is resolved geometrically. Crystal plasticity models have been implemented elsewhere to study shock loading of the energetic materials cyclotetramethylene tetranitramine (HMX) (*19*) and pentaerythritol tetranitrate (PETN) (*20, 21*). Aims of the present work are to develop and implementent a crystal plasticity model for RDX.

The single crystal elastic-plastic model developed in the present work extends the general framework of Becker (*22*) formulated for cubic crystals loaded to possibly high pressures. Here, the model is applied to crystals with orthorhombic symmetry characteristic of RDX. Anisotropic elastic constants and pressure-dependent compressibility are obtained from the experimental literature (*1, 2, 23*). Six slip systems (from four different families of systems) are implemented following analysis of indentation loading profiles and surface impressions (*3, 10*). The model is applied to study indentation, with a spherical indenter, of (001), (021), and (210) faces of single crystals of RDX. Results are compared with numerical predictions from nonlinear isotropic elasticity and analytical isotropic elastic (i.e., Hertzian) solutions. Critical shear strengths associated with slip initiation are assigned upon comparison of results with load excursion data from experiments (*3*). Bulk slip system activity is quantified, and residual surface slip activity is compared with experimental observations.

This report is organized as follows. Constitutive theory and material properties are described in section 2. Indentation simulations are reported in section 3. Conclusions follow in section 4. Notation of continuum mechanics is used. Boldface type is used for vectors and tensors, which are referred to a fixed Cartesian coordinate frame in the reference and current configurations.

2. Theory

A general theory for mechanical behavior of elastic-plastic single crystals is developed in section 2.1. Features and requisite properties particular to RDX are listed in section 2.2.

2.1 Single Crystal Model

Let $\boldsymbol{x} = \boldsymbol{\chi}(\boldsymbol{X}, t)$ denote the motion of material points of the body. The deformation gradient is

$$\nabla\boldsymbol{\chi} = \boldsymbol{F} = \boldsymbol{F}^E\boldsymbol{F}^P, \tag{1}$$

where $\nabla(\cdot)$ denotes the material gradient (i.e., $F_{aA} = \nabla_A\chi_a = \partial x_a/\partial X_A$ in component notation), $\boldsymbol{F}^E$ denotes thermoelastic deformation of the crystal lattice, and $\boldsymbol{F}^P$ represents plastic deformation due to slip. Let a superposed dot denote the material time derivative (i.e., $\partial/\partial t$ at fixed $\boldsymbol{X}$), and let superscript -1 denote inversion. The spatial velocity gradient is

$$\nabla\dot{\boldsymbol{\chi}}(\nabla\boldsymbol{\chi})^{-1} = \dot{\boldsymbol{F}}\boldsymbol{F}^{-1} = \dot{\boldsymbol{F}}^E\boldsymbol{F}^{E-1} + \boldsymbol{F}^E\boldsymbol{L}^P\boldsymbol{F}^{E-1}, \tag{2}$$

where the plastic velocity gradient associated with slip rates $\dot{\gamma}^k$, reference slip directions $\boldsymbol{s}_0^k$, and reference slip plane normals $\boldsymbol{m}_0^k$ on slip systems k is

$$\boldsymbol{L}^P = \dot{\boldsymbol{F}}^P \boldsymbol{F}^{P-1} = \sum_k \dot{\gamma}^k \boldsymbol{s}_0^k \otimes \boldsymbol{m}_0^k. \tag{3}$$

The tensor product is $\otimes$. Slip system geometry is pushed forward to the current configuration via

$$\boldsymbol{s}^k = \boldsymbol{F}^E \boldsymbol{s}_0^k, \qquad \boldsymbol{m}^k = \boldsymbol{F}^{E-\mathrm{T}} \boldsymbol{m}_0^k, \tag{4}$$

where superscript T denotes the transpose. From the orthonormality of slip directions and slip plane normals, plastic deformation is isochoric:

$$\dot{\overline{\det \boldsymbol{F}^P}} = \det \boldsymbol{F}^P \mathrm{tr} \boldsymbol{L}^P = 0, \qquad J = \det \boldsymbol{F} = \det \boldsymbol{F}^E > 0. \tag{5}$$

The trace of a second-order tensor is denoted by $\mathrm{tr}(\cdot)$. By the polar decomposition theorem, let the thermoelastic deformation be split as follows:

$$\boldsymbol{F}^E = \boldsymbol{R}^E \boldsymbol{U}^E, \quad \boldsymbol{U}^E = \boldsymbol{U}^{E\,\mathrm{T}}, \quad \boldsymbol{R}^{E-1} = \boldsymbol{R}^{E\,\mathrm{T}}, \quad \det \boldsymbol{R}^E = 1. \tag{6}$$

A logarithmic thermoelastic strain measure is defined as

$$\boldsymbol{\varepsilon} = \ln \boldsymbol{U}^E = \frac{1}{2} \ln(\boldsymbol{F}^{E\,\mathrm{T}} \boldsymbol{F}^E), \qquad \mathrm{tr}\boldsymbol{\varepsilon} = \ln[\det(\boldsymbol{U}^E)] = \ln J. \tag{7}$$

The logarithmic thermoelastic strain is split into deviatoric and volumetric parts as

$$\boldsymbol{\varepsilon} = \boldsymbol{\varepsilon}' + \frac{1}{3} \bar{\varepsilon} \boldsymbol{1}, \qquad \bar{\varepsilon} = \mathrm{tr}\boldsymbol{\varepsilon} = \ln J, \tag{8}$$

where $\boldsymbol{1}$ is the second-order unit tensor. Note that $\bar{\varepsilon} = 0$ when $J = 1$. Let $\boldsymbol{\sigma}$ denote the usual Cauchy stress tensor. The stress tensor in the deformed but unrotated crystal coordinate system is

$$\boldsymbol{S} = \boldsymbol{R}^{E-1} \boldsymbol{\sigma} \boldsymbol{R}^E. \tag{9}$$

The nonlinear elastic component of the model follows (*22*). Henceforward, only the isothermal case is considered, since isothermal conditions are an appropriate assumption for applications of the model discussed in section 3. Let the unrotated stress be split into deviatoric and hydrostatic parts:

$$\boldsymbol{S} = \boldsymbol{S}' + \bar{S} \boldsymbol{1}, \qquad \bar{S} = \frac{1}{3} \mathrm{tr} \boldsymbol{S} = \frac{1}{3} \mathrm{tr} \boldsymbol{\sigma} = -p, \tag{10}$$

with p the Cauchy pressure. The following operator extracts the deviatoric part of a second-order tensor:

$$\mathbb{I}' = \mathbb{I} - \frac{1}{3}\mathbf{1}\otimes\mathbf{1}, \qquad \mathbb{I}'_{ABCD} = \delta_{AC}\delta_{BD} - \frac{1}{3}\delta_{AB}\delta_{CD}. \tag{11}$$

The constitutive equations for the deviatoric stress and pressure are (*22*)

$$\boldsymbol{S}' = \mathbb{I}' : \mathbb{C} : \boldsymbol{\varepsilon}' + \frac{1}{3}(\mathbb{I}' : \mathbb{C} : \mathbf{1})\bar{\varepsilon}, \tag{12}$$

$$p = \frac{B_0}{B'}[\exp(-B'\bar{\varepsilon}) - 1] - \frac{1}{3}\boldsymbol{\varepsilon}' : \mathbb{C} : \mathbf{1}. \tag{13}$$

Here, B_0 and B' are the reference bulk modulus and the pressure derivative of the bulk modulus, and $\mathbb{C}$ is the tensor of second-order elastic constants, referred to the (unrotated) crystal frame. The colon denotes contraction over two pairs of indices, e.g., $(\mathbb{C} : \boldsymbol{\varepsilon}')_{AB} = \mathbb{C}_{ABCD}\varepsilon'_{CD}$. Pressure dependence of shear elastic coefficients implemented elsewhere for cubic crystals (*22*) is omitted in equation 13 because of limited experimental data for the material of present interest.

The second term on the right side of equation 12 accounts for possible effects of volume changes on deviatoric stress in anisotropic crystals. The second term on the right side of equation 13 accounts for possible effects of deviatoric strains on pressure in anisotropic crystals. Viscoelastic effects are omitted.

The flow rule for slip is (*22*)

$$\tau^k = \boldsymbol{\sigma} : (\boldsymbol{s}^k \otimes \boldsymbol{m}^k) = \tau_0^k \left[\frac{|\dot{\gamma}^k| + \xi}{\dot{\gamma}_0}\right]^m \operatorname{sgn}(\dot{\gamma}^k). \tag{14}$$

The resolved shear stress on slip system k is τ^k. Material parameters are initial and constant slip strength τ_0^k for each slip system, reference strain rate $\dot{\gamma}_0$, and rate sensitivity m. Constant $\xi \ll \dot{\gamma}_0$ provides a finite strength at zero strain rate and is included for numerical reasons. Strain hardening is omitted in equation 14 because sufficient data do not exist to construct more complex slip system constitutive equations for the material of present interest.

2.2 RDX

Physical properties of RDX single crystals are listed in table 1. This description is restricted to the α phase, which is the stable polymorph for pressures under ≈ 3.8 GPa and temperatures under ≈ 480 K. High pressure phases with different structures (γ, β) and melting at higher temperatures are not considered relevant to this application and are discussed elsewhere (*15*).

Table 1. Structural and physical properties of RDX single crystals (ambient) .

Property	**Value**	**Reference**
Space group	*Pbca*	(*10*)
Crystal structure	orthorhombic	
Lattice parameters [nm]	$a = 1.3182$ $b = 1.1574$ $c = 1.0709$	(*10*)
Mass density [g/cm^3]	1.806	(*2*)

Elastic properties are listed in table 2, obtained from experiments. Isentropic second-order elastic constants (*1, 2*) and the bulk modulus have been converted to isothermal values at 295 K via the usual thermodynamic formulae (*24*) incorporating anisotropic thermal expansion (*25*) and specific heat (*17*). Voigt's notation is used, i.e., $\mathbb{C}_{ABCD} \leftrightarrow C_{\alpha\beta}$, where Greek indices $1, 2, \ldots, 6$. Voigt (G_V) and Reuss (G_R) bounds (*24, 26*) on the effective shear modulus are also listed. Differences between Voigt and Reuss bounds for the bulk modulus B_0, on the order $1-3\%$, are considered insignificant.

Table 2. Isothermal second-order elastic constants of RDX single crystals (ambient).

Property	**Value** (*1*)	**Value** (*2*)
C_{11} [GPa]	24.56	36.48
C_{22} [GPa]	18.85	24.49
C_{33} [GPa]	17.33	20.78
C_{12} [GPa]	7.61	0.90
C_{13} [GPa]	5.30	1.26
C_{23} [GPa]	5.24	8.16
C_{44} [GPa]	5.15	11.99
C_{55} [GPa]	4.06	2.72
C_{66} [GPa]	6.90	7.68
B_0 [GPa]	10.5	11.2
G_V [GPa]	6.06	9.26
G_R [GPa]	5.72	6.40

As is evident from values listed in table 2, second-order elastic constants reported for different sets of experiments on single crystals of RDX can vary substantially. Values obtained using

resonant ultrasonic methods listed in table 2 (*1*) are in reasonably close agreement with those reported by other researchers using the same method (*27*). Values obtained using Brillouin scattering (*2*) listed in table 2 are notably different, with particularly larger shear stiffness. Values obtained using a third technique, impulsive stimulated thermal scattering (*28*), are similar to those obtained using resonant ultrasound spectroscopy. Values obtained using empirical atomic models (*18, 29*) also display differences among one another and differences with those obtained in experiments.

In this work, the two sets of elastic constants of Haussuhl (*1*) and Haycraft et al. (*2*) are used because these are the softest and stiffest reported experimental measurements, respectively; results obtained using these two sets are thought to provide an indication of the most and least compliant expected response. Results obtained using the constants of Haussuhl (*1*) are very similar to those that would be obtained using values from Schwarz et al. (*27*) and Sun et al. (*28*).

Pressure and temperature dependencies of second-order elastic coefficients have been calculated using molecular dynamics (*29*); however, these predicted values have not been validated using experiments, and some discrepancies exist among calculated second-order elastic constants at room temperature and experimental values (*2*). For this reason, in this study the nonlinear elastic model only incorporates pressure dependence of the compressibility (i.e., the bulk modulus) obtained experimentally and not that of all elastic coefficients. The value used here is $B' = 6.95$ (*23, 30*).

Potential slip systems in RDX–as identified from hardness versus orientation profiles (*10*), indentation force versus depth data (*3, 11*), and residual surface impressions from indentation (*3*)–are listed in table 3. Slip system geometry is referred to a Cartesian system with axes (X_1, X_2, X_3) parallel to lattice vectors $(\boldsymbol{a}, \boldsymbol{b}, \boldsymbol{c})$. These slip systems are illustrated in figure 1.

Table 3. Slip systems in RDX single crystals (indentation).

System k	**Miller indices**	$\boldsymbol{m}_0$	$\boldsymbol{s}_0$	**Maximum strength [GPa]**	**Reference**
1	$(021)[100]$	(0,0.880,0.475)	[1,0,0]	0.885	(*3, 10*)
2	$(0\bar{2}1)[100]$	(0,-0.880,0.475)	[1,0,0]		
3	$(011)[100]$	(0,0.679,0.734)	[1,0,0]	0.645	(*3, 10*)
4	$(0\bar{1}1)[100]$	(0,-0.679,0.734)	[1,0,0]		
5	$(010)[100]$	(0,1,0)	[1,0,0]	0.885	(*3*)
6	$(010)[001]$	(0,1,0)	[0,0,1]	0.885	(*3, 10*)

Listed initial slip system strengths are upper bounds obtained from analysis of load excursion data

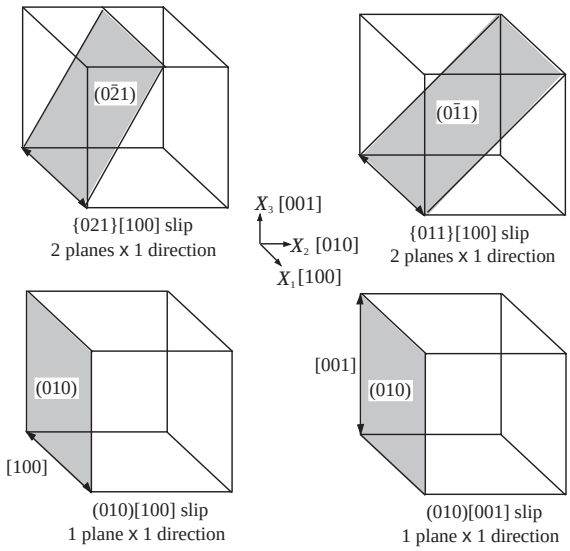

Figure 1. Slip systems in RDX single crystals (unit cell parameters not to scale).

using the analytical Hertzian solution for frictionless spherical indentation into a semi-infinite, linear elastic, isotropic material. It is noted that other systems may become active (and those listed may become inactive) for loading regimes involving very different pressures, temperatures, and/or strain rates. For example, molecular dynamics simulations (*12*) suggest that partial dislocation loops may glide on (001)[010] during shock loading to pressures in excess of ≈ 1 GPa.

In numerical simulations of section 3, shear strengths for various families of systems are varied parametrically between physically reasonable bounds on the order of the theoretical strength as suggested in the literature (*3, 11*), where $G = G_R = 6.4$ GPa (*2*). These and other parameters are listed in table 4. Reference strain rate $\dot{\gamma}_0$ is on the order of the plastic slip rate experienced during indentation simulations described later, and the very small value of rate sensitivity m provides for a nearly rate insensitive response, the simplest numerically pragmatic assumption in the absence of experimental data enabling calibration of this material parameter.

Table 4. Crystal plasticity model parameters for RDX.

Property	**Value**
τ_0^k	$G/40 \lesssim \tau_0^k \lesssim G/10$
m	5×10^{-3}
$\dot{\gamma}_0$	10^{-2} /s
ξ	10^{-7} /s

3. Indentation

The indentation boundary value problem and numerical aspects are described in section 3.1. Results for indentation of RDX with slip suppressed (i.e., nonlinear anisotropic elasticity) are reported in section 3.2. Results for indentation of RDX with slip enabled are reported in section 3.3.

3.1 Boundary Value Problem

The constitutive model presented in section 2 is implemented in the `ALE3D` multi-physics code. Simulations of indentation are performed using an implicit solver for static equilibrium (i.e., no inertial terms in the balance of linear momentum).

The problem geometry is intended to mimic previous experimental studies (*3, 11*). A spherical diamond indenter of radius R, with a nominal value of $R = 1.482$ μm, is used to indent a flat surface of a single crystal of RDX of variable lattice orientation. Diamond is represented as an isotropic nonlinear elastic material with properties listed in table 5.

Table 5. Isotropic elastic properties of diamond indenter.

Property	**Value**	**Reference**
B_0 [GPa]	443	(*31*)
G_V [GPa]	538	
B'	4.0	(*32*)

Following Nowak et al. (*33*), the substrate is represented by a right circular cylinder. The cylinder is assigned a height and radius of $2R$; further increases in dimensions of the cylinder did not affect results of interest. The indenter is modeled as a half-sphere. Each body (i.e., indenter and substrate) is discretized using eight-node hexahedral elements with selective reduced integration; the entire problem consists of ≈ 55000 finite elements. The mesh of the substrate is highly refined in the vicinity of contact beneath the indenter, where stress fields are inhomogeneous, and the mesh coarsens progressively with distance from the initial contact point. Simulations with smaller elements demonstrated that further increases in mesh refinement did not affect results of interest. Anisotropic crystal plasticity simulations were also performed with the original cylindrical mesh rotated by $\pi/4$ about the X_3 axis (i.e., Z-axis) with the initial crystal lattice orientation held fixed; nearly identical results were obtained for plastic slip contours,

demonstrating that strain localization was not artificially sensitive to mesh construction.

During the loading phase, the upper face of the half-spherical indenter is assigned a constant (downward) velocity of $\dot{D} = 10$ nm/s, leading to strain rates similar to those of experiments (*3*). The lower face of the cylinder is rigidly fixed, while the lateral sides (circumference) are traction free. The indentation depth is denoted by D; actual depth d of the tip of the sphere in contact with the surface is monitored as an outcome of the numerical solution procedure. Only for a rigid indenter would $d = D$. Indentation force P is defined as the sum of nodal forces along the upper face of the half sphere acting in the direction of D, i.e., the sum of forces work conjugate to the prescribed nodal velocities.

In most of the simulations, contact between indenter and substrate is assumed frictionless, following previous studies that rely on analytical solutions (*3, 11*). In some simulations discussed later, unloading is also performed, whereby after a peak depth is attained, the upper face of the indenter is assigned an upward velocity of $\dot{D} = 10$ nm/s until contact is released. If plastic deformation has occurred, some residual deformation remains in the substrate upon unloading.

Comparison of simulation results (and published experimental results) with the available analytical solution proves useful. The Hertzian solution for spherical indentation of a linear elastic isotropic half space is (*3*)

$$P = \frac{4}{3} E_r R^{1/2} d^{3/2}, \tag{15}$$

where the reduced elastic modulus is

$$E_r = [(1-\nu_i^2)/E_i + (1-\nu_s^2)/E_s]^{-1}, \tag{16}$$

with ν_i (ν_s) and E_i (E_s) denoting Poisson's ratio and Young's modulus, respectively, of the indenter (substrate). In the present context, these are computed from B_0 and G using the standard formulae (*24*). The solution is fairly insensitive to properties of diamond because its stiffness exceeds that of RDX by 1–2 orders of magnitude. It is noted that equation 15 neglects nonlinear aspects of the solution associated with large changes in geometry and nonlinear material behavior (e.g., finite volume and shape changes and nonlinear elastic material properties). Effects of anisotropy and plasticity are, of course, also omitted in the analytical solution.

Simulations of indentation onto (001), (021), and (210) planes are reported in the following. Rotation matrices and second-order elastic constants associated with these crystal orientations are listed in the appendix.

3.2 Elastic Indentation

Isotropic elastic simulations are considered first in order to facilitate comparison with the analytical solution, equation 15. Figures 2 and 3 show indentation force, P, versus tip depth, d, for indentation simulations incorporating nonlinear isotropic elasticity with Voigt (G_V) and Reuss (G_R) bounds on the shear modulus. Also shown are predictions using G_R with a constant bulk modulus ($B' = 0$). Results in figure 2 correspond to elastic constants of Haussuhl (*1*); results in figure 3 correspond to elastic constants of Haycraft et al. (*2*). The indenter radius is $R = 1.482$ µm (*3*). Analytical solutions using the same bounds on the shear modulus, and incorporating linear elastic behavior as in equation 15, are also plotted. As expected, force is larger when the larger shear modulus (G_V) is used. For tip depth $d \gtrsim 50$ nm, the pressure dependence of the bulk modulus causes an increase in force relative to the case with $B' = 0$.

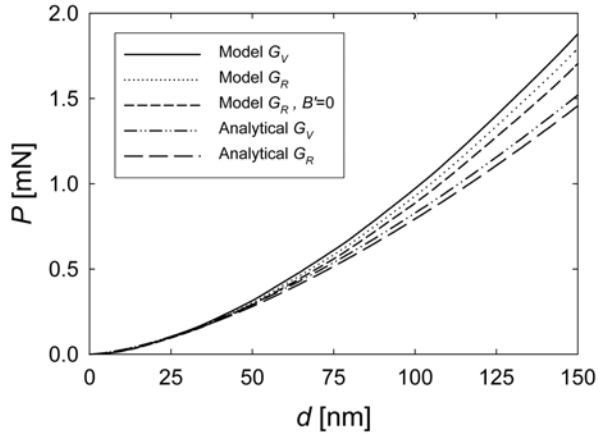

Figure 2. Indentation force vs. tip depth: isotropic elastic simulation results and analytical solutions, $R = 1.482$ µm, elastic constants of Haussuhl (*1*).

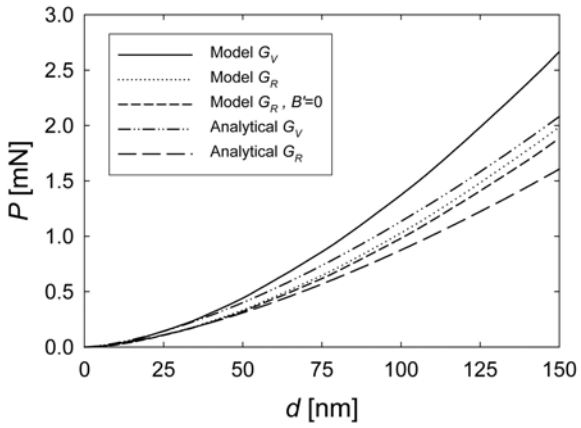

Figure 3. Indentation force vs. tip depth: isotropic elastic simulation results and analytical solutions, $R = 1.482$ μm, elastic constants of Haycraft et al. (*2*).

Differences between analytical and numerical solutions become noticeable for $d \gtrsim 50$ nm when G_R is used, and for $d \gtrsim 40$ nm when G_V is used. In both cases, numerical predictions are stiffer than corresponding analytical solutions. Differences between numerical and analytical solutions are attributed to the following features resolved by the calculation that are not included in the analytical solution: (1) geometric nonlinearities associated with problem geometry, (2) finite logarithmic deviatoric strain measures and true volume changes, (3) nonlinear compressibility for cases with $B' > 0$, and (4) finite size of the substrate. Recall from discussion in section 3.1 that mesh construction did not influence results such as indentation force P; differences between numerical and analytical solutions are not attributed to mesh resolution. All results discussed hereafter involve nonlinear compressibility.

Closer agreement between the numerical model (with constant bulk modulus) and linear elastic analytical solutions can be obtained by the transformation $d \rightarrow d + \delta$ in the analytical solution of equation 15, where δ is a correction that accounts for the presence of the rigid boundary at a depth $Z = 2R$ from the surface of the substrate:

$$\delta = -\frac{P}{2\pi Z E_s}(3 + \nu_s - 2\nu_s^2). \tag{17}$$

As shown in figure 4, equation 17 yields reasonably close agreement between model and (corrected) analytical solutions, suggesting that differences between numerical predictions and uncorrected analytical solutions may be due, at least in part, to the finite size of the substrate modeled in the simulations. It should be noted that this correction, obtained from the analytical

Boussinesq solution for displacement due to a point force applied to a linear elastic isotropic half-space (*34*), is approximate.

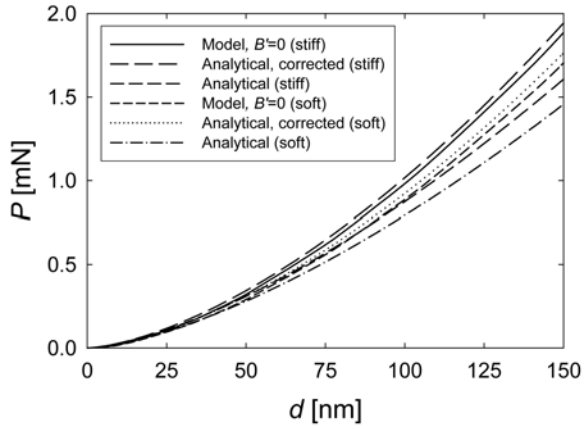

Figure 4. Indentation force vs. tip depth: isotropic elastic simulation results and analytical solutions with and without corrections, $R = 1.482$ μm; soft elastic constants of Haussuhl (*1*) and stiff constants of Haycraft et al. (*2*), Reuss shear modulus.

Results from simulations incorporating isotropic and anisotropic nonlinear elasticity are compared in figures 5 and 6, which show force P versus applied indentation depth D. The indenter radius is $R = 1.482$ μm (*3*). The difference between tip depth d and applied displacement D is $\approx$ 1–2% over the duration of each simulation. Load excursion data thought to correspond to the onset of slip in indentation experiments (*3*) are also shown.

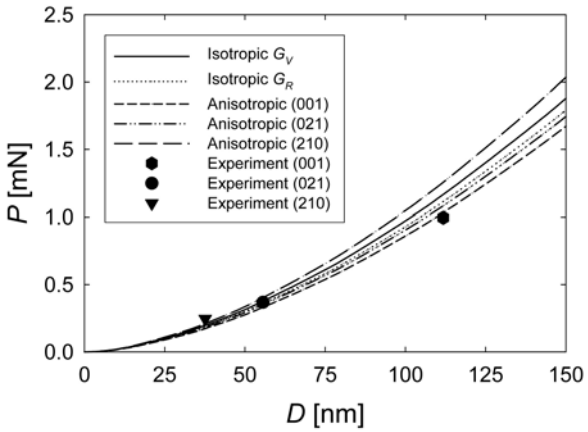

Figure 5. Indentation force vs. applied displacement: isotropic and anisotropic elastic simulation results, and experimental initial load excursion data (*3*), $R = 1.482\,\mu$m, elastic constants of Haussuhl (*1*).

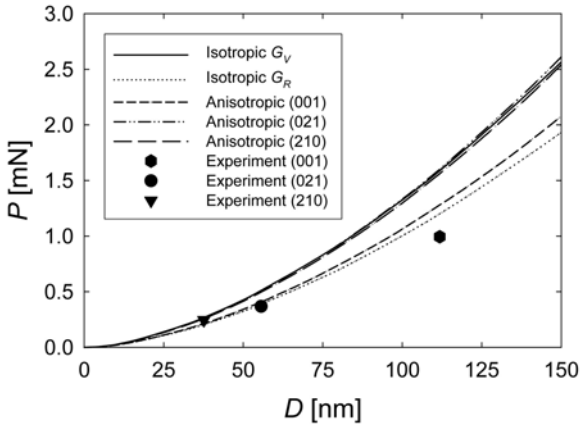

Figure 6. Indentation force vs. applied displacement: isotropic and anisotropic elastic simulation results, and experimental initial load excursion data (*3*), $R = 1.482\,\mu$m, elastic constants of Haycraft et al. (*2*).

First, consider the numerical predictions in figure 5, which are obtained using the relatively compliant elastic constants reported by Haussuhl (*1*). Orientation (210) is relatively stiff, with predicted force P exceeding that of the isotropic case using Voigt shear modulus G_V. Orientation (001) is the most compliant, with predicted force P less than that for the isotropic case using Reuss shear modulus G_R. Simulations predict $P^{(001)} < P^{(021)} < P^{(210)}$. As shown in the appendix, the elastic stiffness component associated with indentation follows the sequence $C_{33}^{(001)} < C_{33}^{(021)} < C_{33}^{(210)}$. Experiments (*3*) suggest that orientation (001) is most compliant, in agreement with the present results. Experiments also suggest that (210) has a higher effective modulus E_r than (021), while (021) has a higher measured hardness than (210). Now compare numerical predictions with experimental data in figure 5. Close agreement between model predictions and load excursion data, within the accuracy of the data, e.g., ≈10–20% uncertainty in measured P (*3*), is demonstrated for all three orientations of the RDX substrate.

Next consider the numerical predictions in figure 6, which are obtained using the relatively stiff elastic constants reported by Haycraft et al. (*2*). Orientations (021) and (210) are relatively stiff, with predicted force P comparable to the isotropic case using Voigt shear modulus G_V. Orientation (001) is relatively compliant, with predicted force P slightly exceeding the isotropic case using Reuss shear modulus G_R. In other words, simulations predict $P^{(001)} < P^{(021)} \approx P^{(210)}$. Next compare numerical predictions with experimental data in figure 6. For the (210) orientation, the load curve from the elastic model coincides with the load excursion data, within the accuracy of the data. Elastic model load curves are significantly stiffer than load excursion data for (001) and (021) orientations. Molecular simulations suggest that all shear moduli of RDX increase with increasing pressure (*29*); incorporation of such effects into the present indentation simulations would seem to lead to an increase in tangent modulus with increasing depth of indentation, further increasing differences between modeling using constants of Haycraft et al. (*2*) and experiment.

Predictions obtained using each set of elastic constants (*1, 2*) are compared directly for substrate orientations (001), (021), and (210) in figures 7, 8, and 9. Significantly closer agreement between model and experiment (*3*) is obtained from the elastic constants of Haussuhl (*1*) for indentation onto (001) and (021) planes. Comparable accuracy is obtained from either set of elastic constants for indentation on (210) planes. Thus, the present simulations confirm that elastic constants obtained using resonant ultrasonic methods (*1, 27*) provide a more realistic representation of elastic stiffness during nano-indentation than elastic constants obtained from Brillouin scattering (*2*), with the latter appearing too stiff.

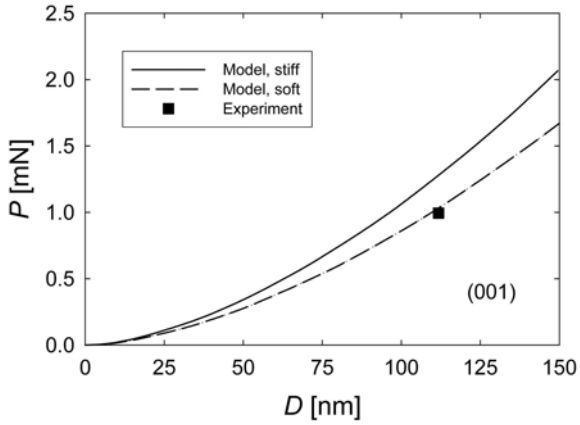

Figure 7. Indentation force vs. applied displacement for elastic indentation onto plane (001): predictions obtained using stiff (*2*) and soft (*1*) elastic constants compared to experiment (*3*).

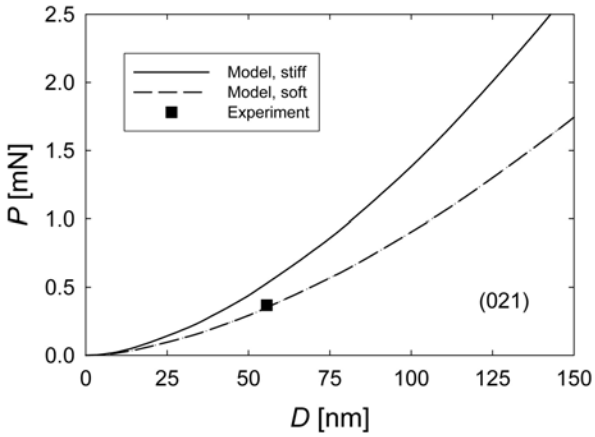

Figure 8. Indentation force vs. applied displacement for elastic indentation onto plane (021): predictions obtained using stiff (*2*) and soft (*1*) elastic constants compared to experiment (*3*).

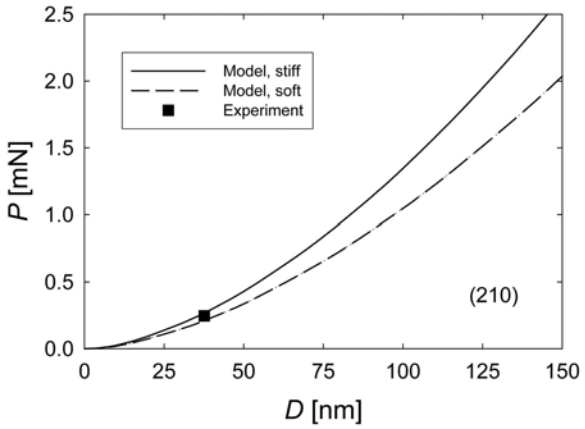

Figure 9. Indentation force vs. applied displacement for elastic indentation onto plane (210): predictions obtained using stiff (*2*) and soft (*1*) elastic constants compared to experiment (*3*).

The influence of indenter radius R on nonlinear anisotropic simulation results is shown in figures 10, 11, and 12; in each case, elastic constants of Haycraft et al. (*2*) are employed. For all three orientations of the RDX substrate, indentation force is nearly proportional to $R^{1/2}$, as in the isotropic linear elastic analytical solution equation 15. For exact $R^{1/2}$ proportionality, the three curves within each of figures 10, 11, and 12 would coincide. This supports the assertion that nonlinearities contribute to differences between numerical and analytical solutions.

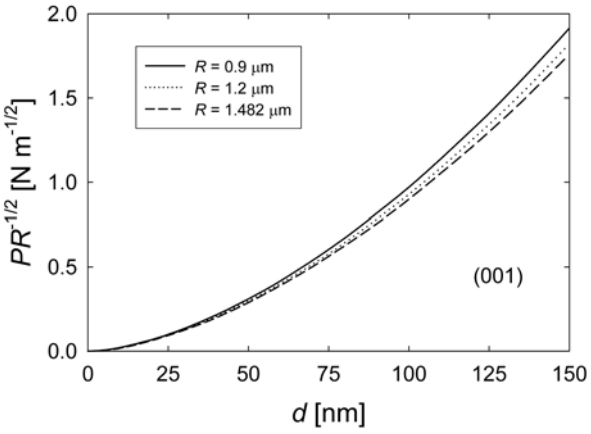

Figure 10. Normalized force vs. tip depth for elastic indentation onto plane (001), elastic constants of Haycraft et al. (*2*).

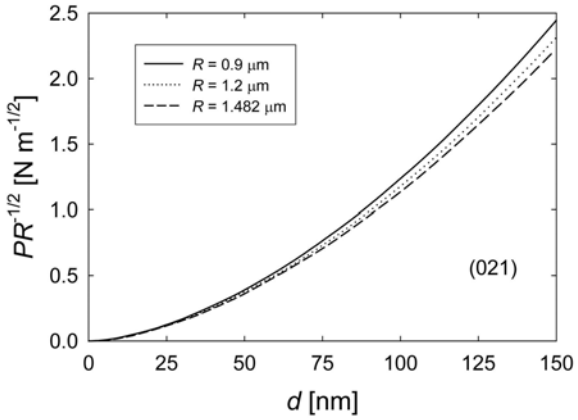

Figure 11. Normalized force vs. tip depth for elastic indentation onto plane (021), elastic constants of Haycraft et al. (*2*).

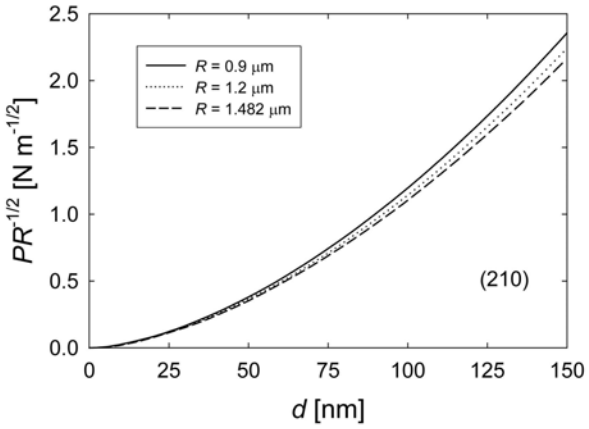

Figure 12. Normalized force vs. tip depth for elastic indentation onto plane (210), elastic constants of Haycraft et al. (*2*).

All simulation results reported in figures in this work are obtained assuming frictionless contact. In order to estimate an upper bound on indentation force for non-negligible sliding friction between indenter and substrate, simulations incorporating nonlinear isotropic elasticity with G_V or G_R of Haycraft et al. (*2*) were also conducted assuming fully tied tangential contact, i.e., no sliding, full sticking, or an infinite friction coefficient. In such simulations, normal separation was permitted. It was found that differences between frictionless and tied contact were insignificant. For example, at $D = 150$ nm, for simulations incorporating G_V, $P = 2.56$ mN for frictionless contact and $P = 2.57$ mN for tied contact. Experimental measurements of dynamic friction for RDX single crystals sliding on a glass substrate (*35*) suggest a friction coefficient on the order of unity for loads under 1 g (≈ 10 mN) wherein contact is characterized as elastic, and a friction coefficient of 0.35 for loads in excess of 10 g, wherein contact is characterized as plastic. Experimental sliding velocities were on the order of 0.2 mm/s. The present indentation simulations consider a different geometry, smaller system sizes (loads under 1 g), and slower sliding velocities (on the order of 10 nm/s), so the reported experimental values for friction coefficients (*35*) may not strictly apply here.

3.3 Elastic-Plastic Indentation

Results are now reported for indentation of RDX single crystals described by the complete nonlinear crystal plasticity constitutive model of section 2. Because strengths of families of slip systems are not known precisely a priori from experiments, shear strengths τ_0^k are varied parametrically over the range listed in table 4. This range, which corresponds to slip resistance on the order of the theoretical strength, is physically descriptive of homogeneous nucleation of

glissile dislocation lines and loops.

Results of indentation force versus applied indention depth are shown in figures 13, 14, and 15. In each of these figures, results correspond to elastic constants of Haycraft et al. (*2*). For situations in which one family (consisting of one or two systems, as in figure 1) is assigned strength $\tau_0^k = G/20$, the remaining systems are assigned strength $G/10$. Recall that Miller indices corresponding to slip system numbers 1–6 are listed in table 3. For indentation on (001), only slip system 6 exhibits significant activity; lowering the strength of any of the other systems 1–5 from $G/10$ to $G/20$ does not noticeably affect indentation force P. For indentation on (021), lowering the strength of system 6 to $G/20$ provides the greatest reduction in indentation force. However, lowering the strength of the other families of systems does produce a slight decrease in force. For indentation on (210), the opposite trend is observed. Lowering the strength of system 6 to $G/20$ produces a small reduction in force, whereas lowering the strength of the other families of systems produces a more substantial reduction.

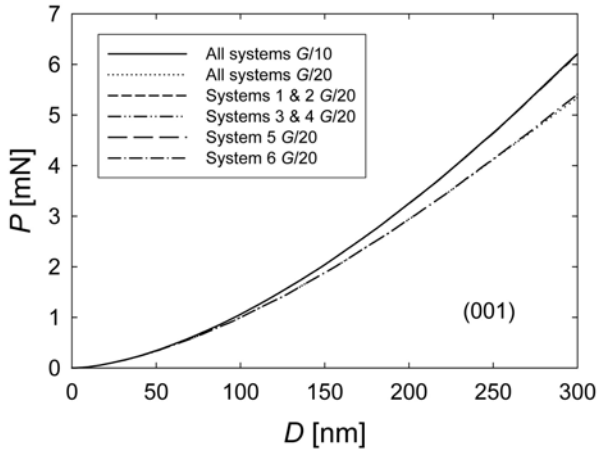

Figure 13. Force vs. depth for elastic-plastic indentation onto plane (001); slip systems have strength $G/10$ unless noted otherwise, elastic constants of Haycraft et al. (*2*).

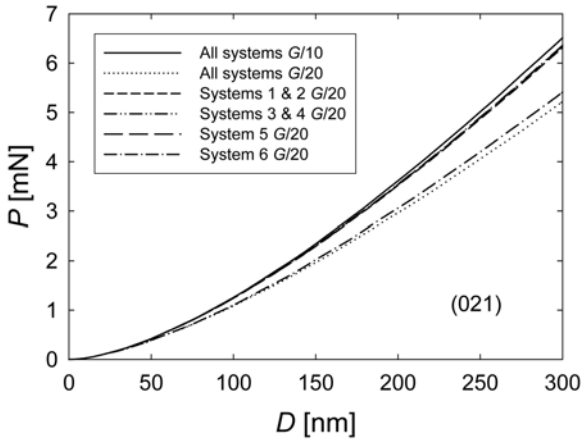

Figure 14. Force vs. depth for elastic-plastic indentation onto plane (021); slip systems have strength $G/10$ unless noted otherwise, elastic constants of Haycraft et al. (*2*).

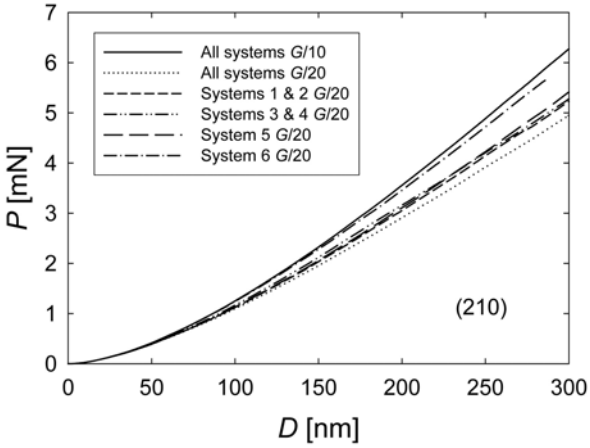

Figure 15. Force vs. depth for elastic-plastic indentation onto plane (210); slip systems have strength $G/10$ unless noted otherwise, elastic constants of Haycraft et al. (*2*).

Model predictions for uniform slip strength $\tau_0^k = G/20$ are compared with experimental data of Ramos et al. (*3*) in figures 16, 17, and 18, with predictions obtained using elastic constants of references (*1*) and (*2*). Predicted forces exceed experimental values at larger indendation depths in each orientation and for both sets of elastic constants. Results corresponding to more compliant elastic constants (*1*) provide closer agreement to experimental values than results corresponding to stiffer elastic constants (*2*).

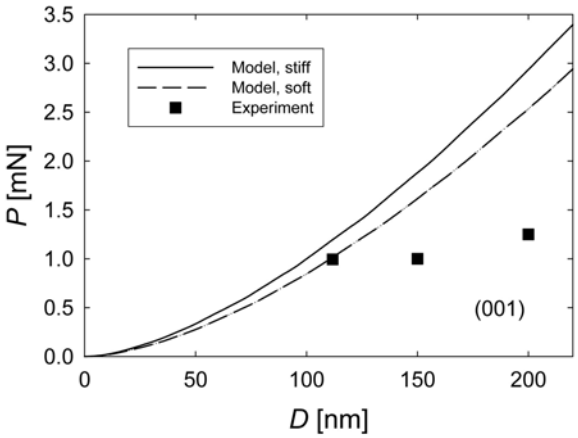

Figure 16. Force vs. depth for elastic-plastic indentation onto plane (001). Model results assume all slip systems have same strength $G/20$; predictions obtained using stiff (*2*) and soft (*1*) elastic constants; experimental data (*3*) shown for comparison.

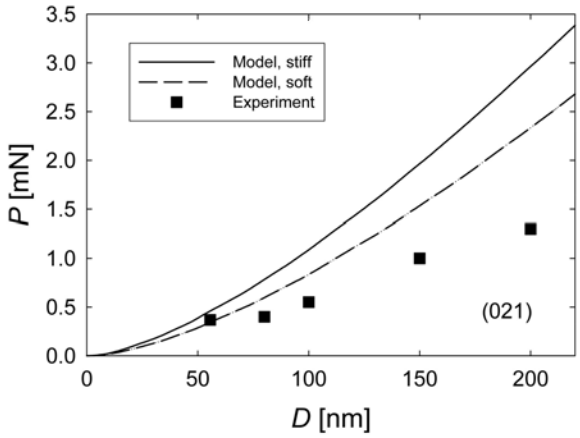

Figure 17. Force vs. depth for elastic-plastic indentation onto plane (021). Model results assume all slip systems have same strength $G/20$; predictions obtained using stiff (*2*) and soft (*1*) elastic constants; experimental data (*3*) shown for comparison.

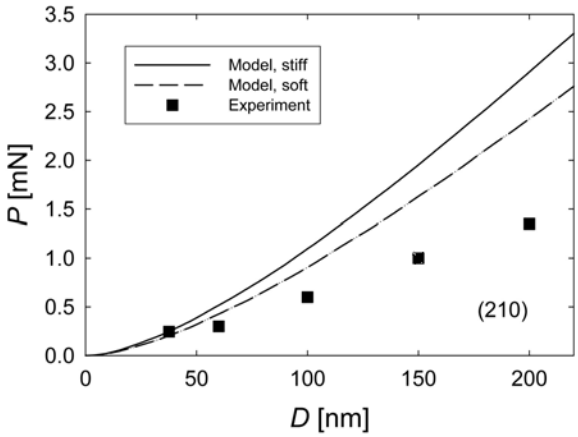

Figure 18. Force vs. depth for elastic-plastic indentation onto plane (210). Model results assume all slip systems have same strength $G/20$; predictions obtained using stiff (*2*) and soft (*1*) elastic constants; experimental data (*3*) shown for comparison.

Model predictions for uniform slip strengths τ_0^k of $G/10$, $G/20$, and $G/40$ are compared with experimental data (*3*) in figures 19, 20, and 21, with predictions obtained using elastic constants of Haycraft et al. (*2*). Further reduction of slip strengths below $G/40$ enables closer agreement with experimental data at larger indentation depths, but also leads to significant under-prediction of the force at smaller depths near initial yield.

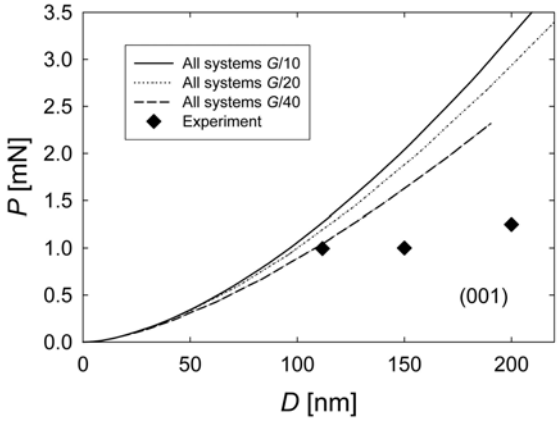

Figure 19. Force vs. depth for elastic-plastic indentation onto plane (001), elastic constants of Haycraft et al. (*2*). Model results assume all slip systems have same strength; experimental data (*3*) shown for comparison.

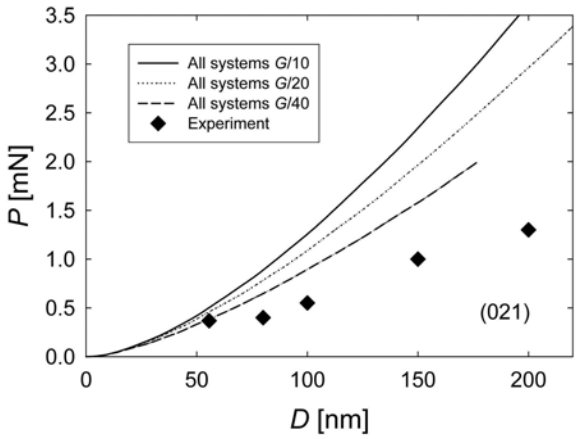

Figure 20. Force vs. depth for elastic-plastic indentation onto plane (021), elastic constants of Haycraft et al. (*2*). Model results assume all slip systems have same strength; experimental data (*3*) shown for comparison.

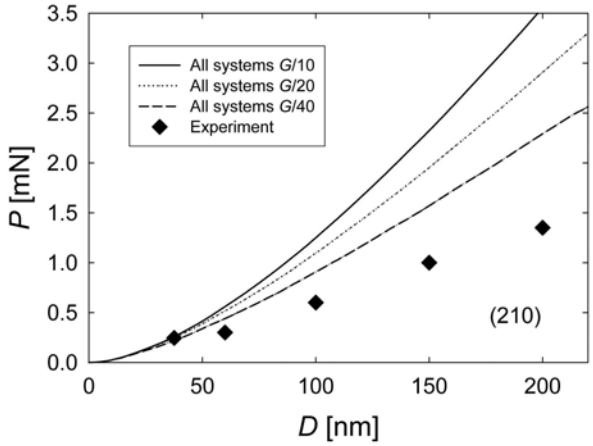

Figure 21. Force vs. depth for elastic-plastic indentation onto plane (210), elastic constants of Haycraft et al. (*2*). Model results assume all slip systems have same strength; experimental data (*3*) shown for comparison.

As noted in section 3.2, uncertainty in the true tip radius R of the indenter could lead to discrepancies between simulations and experiments. Also noted in section 3.2, surface fractures and/or subsurface fractures could contribute to a loss of stiffness that would be reflected only in the experimental data. RDX is prone to cleavage fracture on planes (001), (010), (001), (241), and $(2\bar{4}1)$ (*3, 7, 9*). Experimental data demonstrate nearly horizontal steps in force versus displacement corresponding to discrete slip (and possibly fracture) events that are not readily resolved by a constant strength continuum crystal plasticity model such as the one formulated here.

Details of slip system interactions and pressure dependence of shear strength are omitted in the present model. Indentation experiments have suggested the importance of cross slip (*3*), and atomic modeling has noted that different slip mechanisms may become important at high pressures (*12*). Incorporation of these effects into a more complex slip model might provide closer agreement with experiment, e.g., if glide resistance were to decrease with pressure, since local pressures under the indenter achieve several GPa, as will be shown later. Atomic modeling (*12, 36*) may provide insight into dependence of slip resistance on pressure (and temperature, etc.) not available from experimental methods.

In subsequent figures presented in this work, elastic constants obtained from resonant ultrasound spectroscopy (*1*) are used, and all systems are assigned a strength of $\tau_0^k = G/20 = 0.32$ GPa. The intent is not necessarily reproduction of experimental force-displacement data, but rather to deduce activity of which slip system(s) is most prominent for indentation on particular planes. The present crystal plasticity simulations enable direct quantification of surface and subsurface slip on each system. In contrast, hardness or indentation experiments (*3, 10, 11*) require significant interpretation of data to deduce slip activity and do not provide a quantitative measure of the relative contributions of each slip system to the overall plastic strain field. In the aforementioned experiments, visual observations of slip traces are restricted to residual surface profiles, whereas simulations enable visualization of subsurface slip activity.

Simulations demonstrated sufficient mesh refinement for elastic-plastic simulations. In particular, doubling of the number of elements in the mesh resulted in a less than 1% change in P for indentation depths up to 300 nm for all three orientations of the substrate with $\tau_0^k = G/20$ assigned for all k.

Model predictions of cumulative slip for indentation to a depth of $D = 200$ nm onto planes (001), (021), and (210) are shown in figures 22, 23, and 24. Corresponding pressure contours are shown in figures 25, 26, and 27. In each case, a slice along the centerline of the cylinder normal to the

laboratory X_1 axis (i.e., X-axis) is shown. For indentation on (001) and (021) planes the X_1 axis is normal to a (100) plane; for indentation on (210) the X_1 axis is approximately normal to a $(2\bar{3}0)$ plane. Cumulative total slip γ is defined as

$$\gamma = \sum_k \gamma^k = \sum_k \int |\dot{\gamma}^k| dt, \tag{18}$$

with γ^k the monotonically increasing cumulative slip on system k. Slip activity is greater for indentation into (021) and (210) planes than for indentation on (001). For this particular viewing plane, slip and pressure contours for indentation on (021) are noticeably asymmetric. Maximum local pressure (but not average pressure) is highest for indentation on (001) despite the lower elastic stiffness for this orientation. The wireframe mesh of the indenter is drawn in each figure; in order to enable clear visualization of heterogeneous slip and pressure distributions in the RDX, the mesh of the substrate, which is considerably more refined than that of the indenter, is not shown.

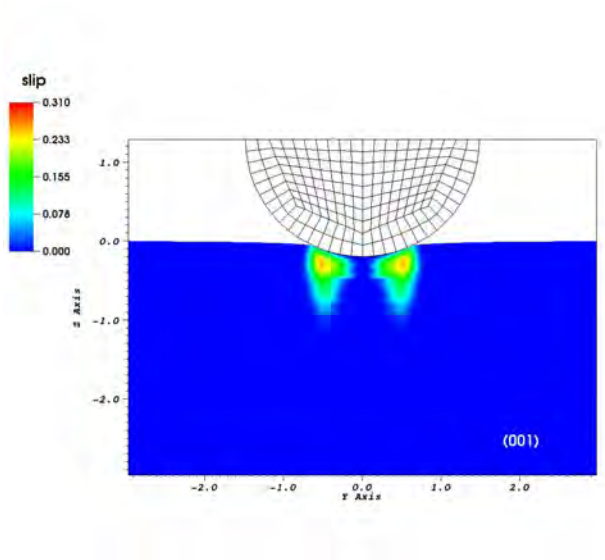

Figure 22. Cumulative total slip contours for indentation to depth $D = 200$ nm onto plane (001); a slice along the centerline of the cylinder normal to the laboratory X_1 axis [i.e., X-axis or (100)] is shown.

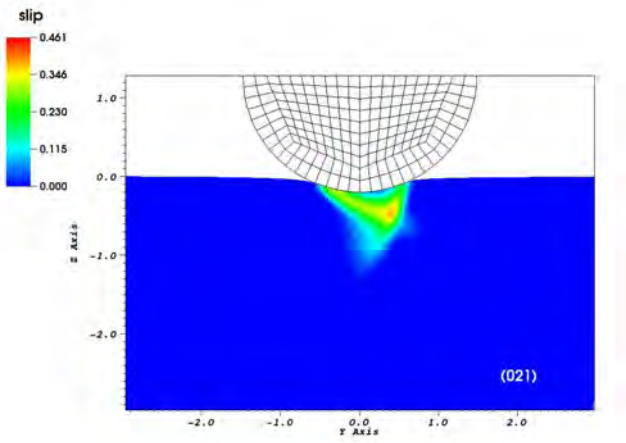

Figure 23. Cumulative total slip contours for indentation to depth $D = 200$ nm onto plane (021); a slice along the centerline of the cylinder normal to the laboratory X_1 axis [i.e., X-axis or (100)] is shown.

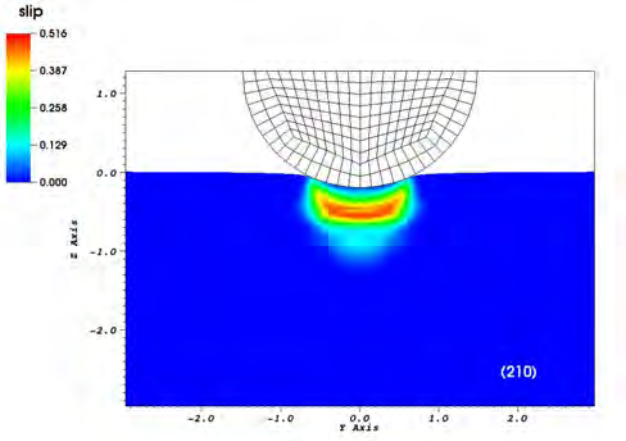

Figure 24. Cumulative total slip contours for indentation to depth $D = 200$ nm onto plane (210); a slice along the centerline of the cylinder normal to the laboratory X_1 axis [i.e., X-axis or $(2\bar{3}0)$] is shown.

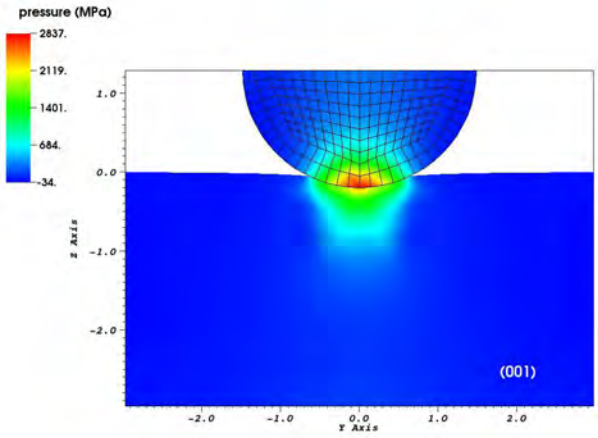

Figure 25. Hydrostatic pressure contours for indentation to depth $D = 200$ nm onto plane (001); a slice along the centerline of the cylinder normal to the laboratory X_1 axis [i.e., X-axis or (100)] is shown.

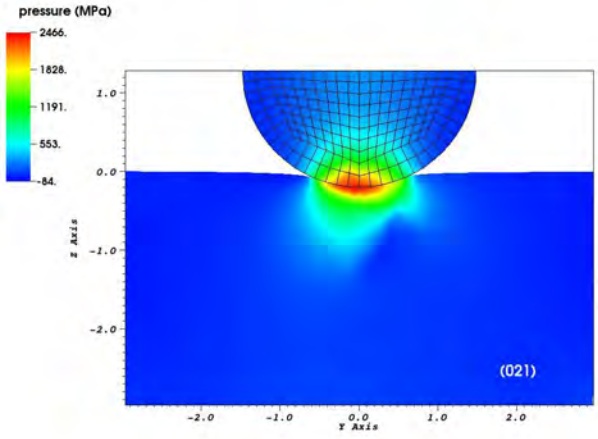

Figure 26. Hydrostatic pressure contours for indentation to depth $D = 200$ nm onto plane (021); a slice along the centerline of the cylinder normal to the laboratory X_1 axis [i.e., X-axis or (100)] is shown.

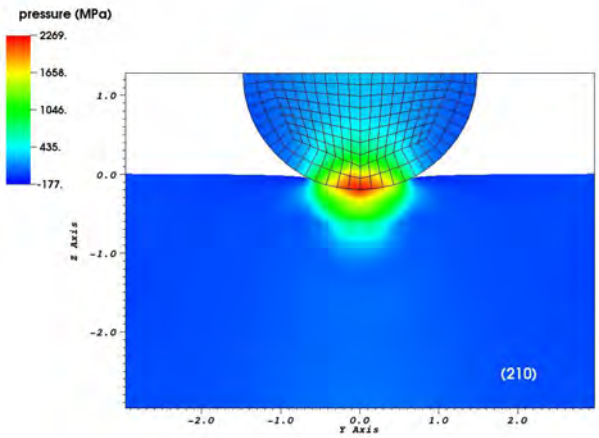

Figure 27. Hydrostatic pressure contours for indentation to depth $D = 200$ nm onto plane (210); a slice along the centerline of the cylinder normal to the laboratory X_1 axis [i.e., X-axis or $(2\bar{3}0)$] is shown.

Tables 6 and 7 list maximum local cumulative slip (i.e., the maximum value of γ^k at any location in the RDX substrate) at an indentation depth $D = 200$ nm when the respective elastic constants of references (*1*) and (*2*) are implemented. Total slip γ listed in the bottom row of each table is not necessarily the sum of all γ^k listed in a given column because the location in the substrate where total slip is maximum does not necessarily correspond to the location where each γ^k is maximum. Consistent with figure 13, orientation (001) exhibits slip primarily on system 6. Significant activity of multiple slip systems is evident for indentation onto (021) and (210) planes. It appears that, for compatibility reasons, slip system 6 is active for indentation on (210) because it is the only system with a slip direction different from [100] (see figure 1 and table 3). Trends are qualitatively similar regardless of choice of elastic constants. Cumulative slip magnitudes are generally slightly larger in table 7 than in table 6 because larger stresses are attained at the same depth of indentation when stiffer elastic constants are prescribed.

Table 6. Maximum local slip γ^k at indentation depth of 200 nm for indentation on (001), (021), and (210) planes, elastic constants of Haussuhl (*1*).

System k	**Plane** (001)	**Plane** (021)	**Plane** (210)
1	0.01	0.19	0.40
2	0.01	0.00	0.40
3	0.08	0.16	0.29
4	0.08	0.00	0.29
5	0.00	0.10	0.51
6	0.31	0.41	0.16
all (γ)	0.31	0.46	0.52

Table 7. Maximum local slip γ^k at indentation depth of 200 nm for indentation on (001), (021), and (210) planes, elastic constants of Haycraft et al. (*2*).

System k	**Plane** (001)	**Plane** (021)	**Plane** (210)
1	0.01	0.19	0.41
2	0.01	0.00	0.41
3	0.06	0.13	0.28
4	0.06	0.00	0.28
5	0.01	0.10	0.52
6	0.35	0.51	0.26
all (γ)	0.35	0.56	0.58

Loading-unloading simulations of indentation on (001), (021), and (210) planes of RDX are performed to enable comparison with experimental observations. Force versus displacement predictions are shown in figure 28 for a single load-unload cycle corresponding to loading to $D \approx 200$ nm and then unloading to $D = 0$. During much of the loading phase, orientation (001) is slightly less stiff than orientations (021) and (210). However, at $D \approx 200$ nm, P is largest for orientation (001). Recall that orientation (001) demonstrates a lower elastic stiffness, but also less slip activity. Hence at larger indentation depths, increased slip activity for orientations (021) and (210) lowers their effective tangent stiffness, and hence P, below that of orientation (001).

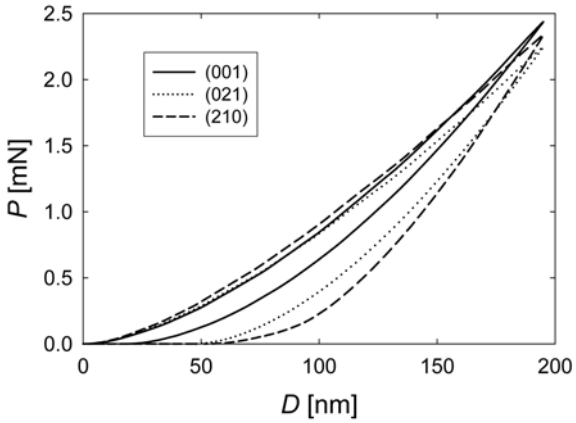

Figure 28. Indentation force vs. applied displacement for a single load-unload cycle on each of (001), (021), and (210) planes.

Hysteresis is also substantially greater for indentation on (021) and (210) than for (001), again demonstrating less slip activity in the latter. Orientation (210) demonstrates the most hysteresis (and greatest slip activity) and the largest elastic stiffness for much of the unloading phase.

Residual cumulative slip contours for indentation to a depth of $D \approx 200$ nm onto planes (001), (021), and (210) are shown in figures 29, 30, and 31. In each case, a slice along the centerline of the cylinder normal to the laboratory X_1 axis (i.e., X-axis) is shown. Contours are similar to those shown in figures 22, 23, and 24, but with greater magnitudes of cumulative slip apparent after unloading on (001) and (210). Recall from equation 18 that cumulative slip can never decrease in time, and slip in forward and reverse directions on a given system both contribute positively; hence, residual slip contours can demonstrate a larger magnitude as a result of any forward or reverse slip occurring during unloading. Cumulative slip shown in figure 30 is exceeded by that in figure 23 since in the former the depth of indentation does not attain 200 nm (figure 28).

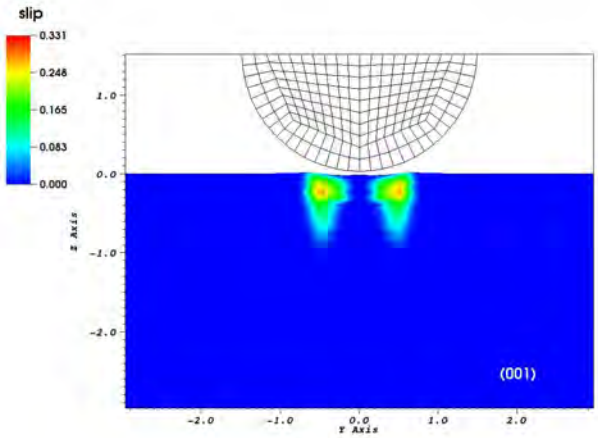

Figure 29. Residual cumulative total slip contours for indentation to depth $D \approx$ 200 nm, followed by unloading, onto plane (001). A slice along the centerline of the cylinder normal to the laboratory X_1 axis [i.e., X-axis or (100)] is shown.

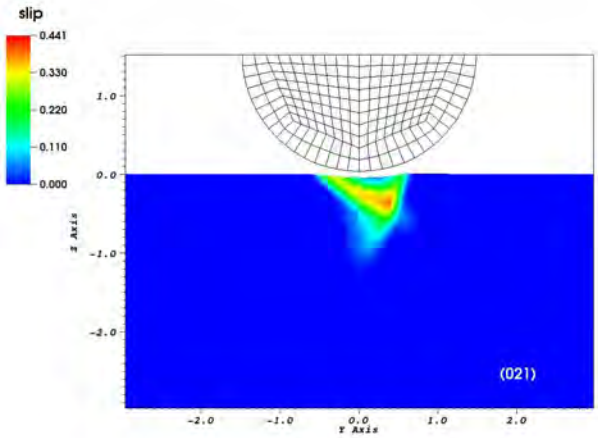

Figure 30. Residual cumulative total slip contours for indentation to depth $D \approx$ 200 nm, followed by unloading, onto plane (021). A slice along the centerline of the cylinder normal to the laboratory X_1 axis [i.e., X-axis or (100)] is shown.

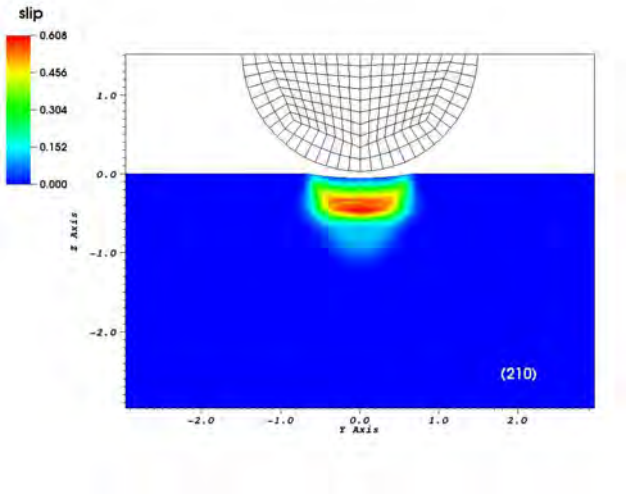

Figure 31. Residual cumulative total slip contours for indentation to depth $D \approx$ 200 nm, followed by unloading, onto plane (210). A slice along the centerline of the cylinder normal to the laboratory X_1 axis [i.e., X-axis or $(2\bar{3}0)$] is shown.

Figures 32–42 show total cumulative slip, γ, and cumulative slip, γ^k, for active individual slip systems on unloaded surfaces of (001), (021), and (210) planes. In each case, the maximum indentation depth prior to unloading is $D \approx 200$ nm. Non-circular contours are consistent with activity of fewer than five geometrically independent systems necessary to accommodate an arbitrary plastic strain field (*3*).

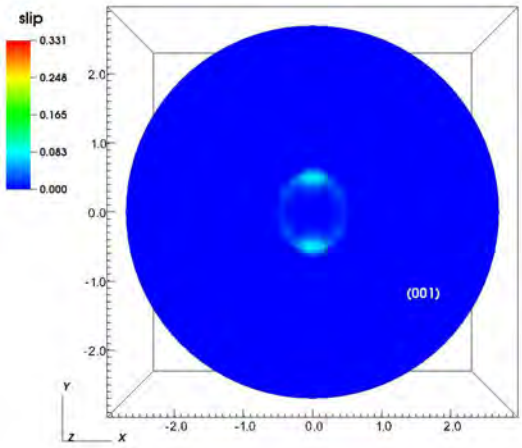

Figure 32. Surface residual cumulative slip contours for indentation to depth $D \approx$ 200 nm, followed by unloading, onto plane (001): total slip.

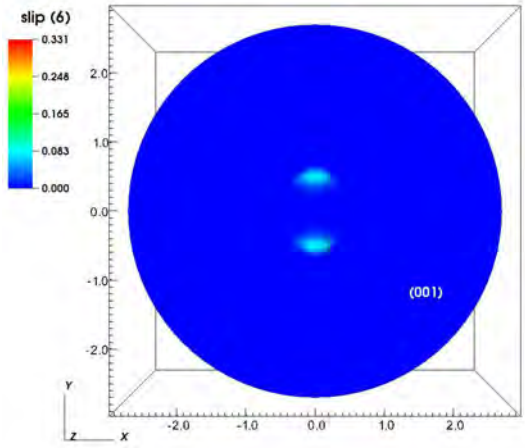

Figure 33. Surface residual cumulative slip contours for indentation to depth $D \approx$ 200 nm, followed by unloading, onto plane (001): slip on system 6 $(010)[001]$.

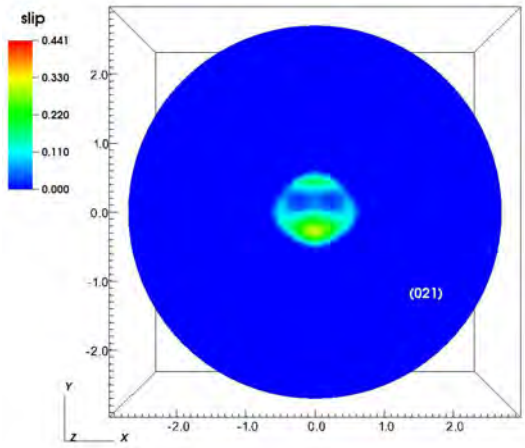

Figure 34. Surface residual cumulative slip contours for indentation to depth $D \approx$ 200 nm, followed by unloading, onto plane (021): total slip.

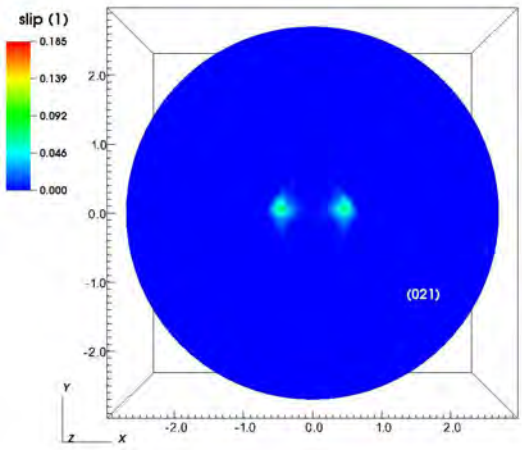

Figure 35. Surface residual cumulative slip contours for indentation to depth $D \approx$ 200 nm, followed by unloading, onto plane (021): slip on system 1 $(021)[100]$.

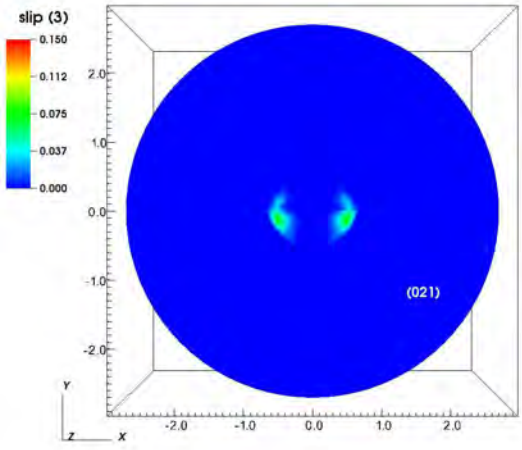

Figure 36. Surface residual cumulative slip contours for indentation to depth $D \approx$ 200 nm, followed by unloading, onto plane (021): slip on system 3 $(011)[100]$.

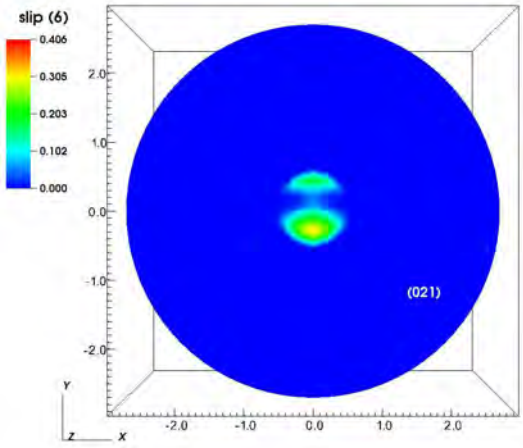

Figure 37. Surface residual cumulative slip contours for indentation to depth $D \approx$ 200 nm, followed by unloading, onto plane (021): slip on system 6 $(010)[001]$.

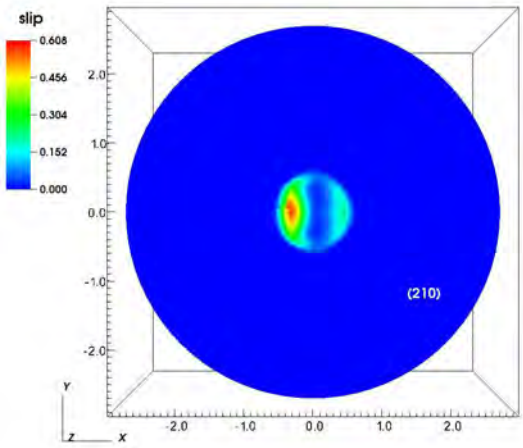

Figure 38. Surface residual cumulative slip contours for indentation to depth $D \approx$ 200 nm, followed by unloading, onto plane (210): total slip.

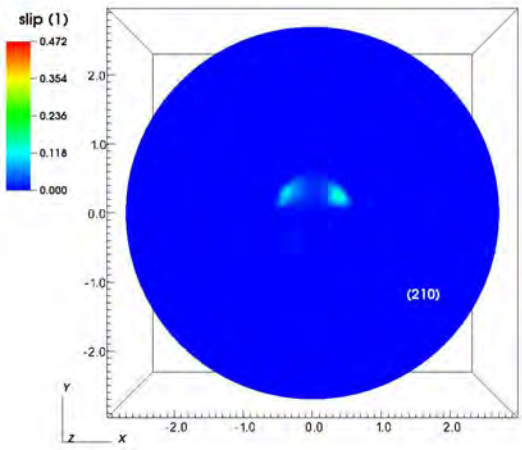

Figure 39. Surface residual cumulative slip contours for indentation to depth $D \approx$ 200 nm, followed by unloading, onto plane (210): slip on system 1 $(021)[100]$.

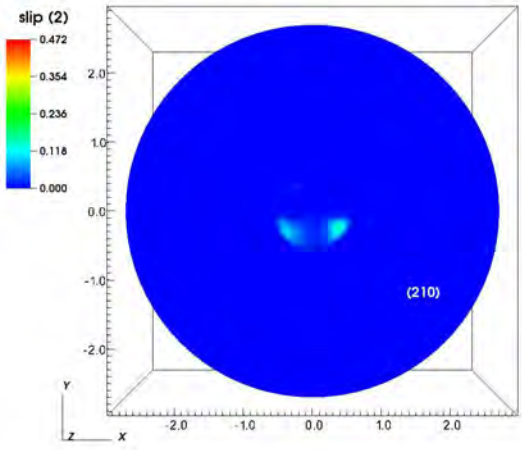

Figure 40. Surface residual cumulative slip contours for indentation to depth $D \approx$ 200 nm, followed by unloading, onto plane (210): slip on system 2 $(0\bar{2}1)[100]$.

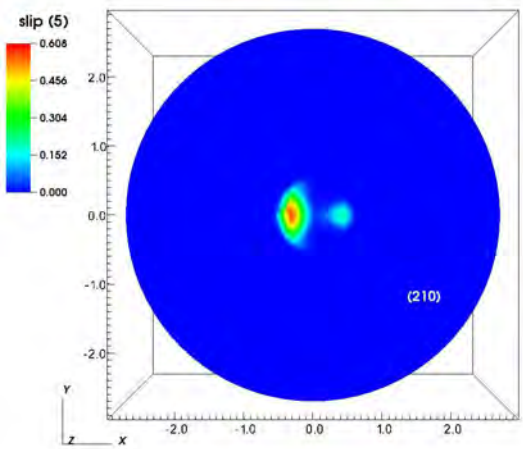

Figure 41. Surface residual cumulative slip contours for indentation to depth $D \approx$ 200 nm, followed by unloading, onto plane (210): slip on system 5 $(010)[100]$.

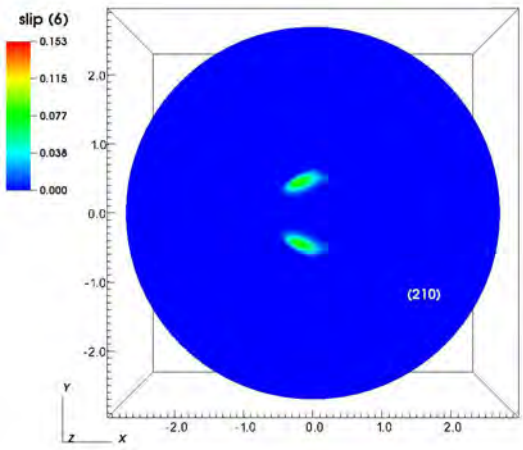

Figure 42. Surface residual cumulative slip contours for indentation to depth $D \approx$ 200 nm, followed by unloading, onto plane (210): slip on system 6 $(010)[001]$.

As shown in figures 32 and 33, surface slip activity results primarily from system 6 for indentation on (001). Slight contributions to the circular total slip trace in figure 32 are due to systems 3 and 4, i.e., $\{011\}[100]$ (not shown). As shown in figures 34–37, surface slip activity is predominantly from system 6, with minor contributions from systems 1 and 3, for indentation on (021). As shown in figures 38–42, surface slip activity is predominantly from system 5, with contributions from systems 1, 2, and 6, for indentation on (210). Faint contributions from systems 3 and 4 (not shown) also occur for indentation on (210).

Active slip planes during the loading history at the specimen surface as predicted by the present simulations are compared with those deduced from experimental surface impressions (*3*) in table 8. It is noted that in simulations of indentation on (210), systems 3 and 4, i.e., $\{011\}[100]$, demonstrate substantial activity within the bulk material (i.e., beneath the surface), but little cumulative slip at the surface. Experiments suggest that $\{011\}[100]$ slip traces exist for indented (210) surfaces of RDX (*3*). Though not presented in this report, predicted residual bulk and surface slip contours were also obtained using the relatively stiff elastic constants of Haycraft et al. (*2*). Trends in results for slip activity were usually qualitatively similar regardless of choice of elastic constants from references (*1*) or (*2*).

Table 8. Significantly active slip planes at the specimen surface during indentation of (001), (021), and (210) planes.

Indentation surface	**Present results**	**Experiment** (*3*)
(001)	(010),{011}	(010),{011},{021}
(021)	(010),(011),(021)	not reported
(210)	(010),{011},{021}	(010),{011},$(02\bar{1})$

4. Conclusions

A nonlinear anisotropic elastic-plastic model has been developed for single crystals of RDX. The model accounts for orthorhombic elastic constants, pressure-dependent compressibility, and dislocation glide on up to six distinct slip systems from four families of crystallographically equivalent slip systems.

Numerical simulations of spherical indentation on (001), (021), and (210) planes of single crystals have been performed. Results show significant influences of elastic anisotropy and elastic nonlinearity on force-displacement data. Model predictions for initial elastic response

using constants measured with resonant ultrasound spectroscopy agree with experimental force-displacement data for indentation on (001), (021), and (210) planes. Model predictions for initial elastic response using constants measured with Brillouin scattering are in reasonable agreement with experiments for indentation on (210), but are stiffer than experiments for indentation on (001) and (021). Orientation (001) is elastically most compliant with respect to indentation force, in agreement with experiments.

Model predictions of force for larger indentation depths, wherein local plastic slip is substantial, tend to exceed experimental values regardless of which set of elastic constants is used. The constant strength (i.e., perfectly plastic) slip model implemented in the present work is unable to replicate nearly horizontal steps in indentation force observed in experiments. Such steps may correspond to discrete slip events of width too fine to be captured by a conventional continuum slip model. Dependencies of shear strength and shear stiffness on slip history and pressure have been omitted; incorporation of such physics, for example, as suggested by atomic simulations, might provide improved agreement. Uncertainties in true indenter tip geometry, and fractures observed in experiments (at the surface) or not observed (subsurface) could also contribute to discrepancies between simulations and experiments.

Critical shear strengths associated with plastic yielding have been estimated on the order of $G/20$, where G is a representative elastic shear modulus. Simulations suggest that slip planes (010) and $\{011\}$ contain active systems for indentation on (001), with slip on system (010)[001] dominating the inelastic response; experimental surface observations confirm that these and $\{021\}$ slip planes may also be active. Simulations suggest that slip planes (010) and $\{021\}$, and to a lesser extent $\{011\}$, are active at the specimen surface for indentation on (210); these same planes have also been confirmed as active in experiments. Simulations suggest that planes (010), (011), and (021) contain active systems for indentation on (021); particular slip planes active for this orientation have not been reported from experimental observations.

The present simulations suggest that system (010)[001] provides the largest contribution to the inelastic material response (i.e., post-yield force versus displacement curve) for indentation on (001) and (021) planes, while five systems $\{021\}[100]$, $\{011\}[100]$, and $(010)[100]$ all contribute to inelastic response for indentation on (210) planes. Plastic deformation and hysteresis are more extensive for indentation on (021) and (210) than for indentation on (001).

Since much plastic deformation occurs in the bulk of the material, and since different slip mechanisms may be prominent at the surface and in the bulk, these results offer new insight into inelastic mechanical behavior of RDX not available from experimental observations of residual

surface topography alone.

In summary, the model developed here, when used with elastic constants obtained from resonant ultrasonic methods, is thought to provide an accurate representation of the nonlinear anisotropic response of RDX single crystals in the elastic regime of indentation. This model is also thought to provide a qualitatively realistic depiction of activity of different slip systems when a uniform and constant shear strength on the order of $G/20$ is prescribed. However, refinements of the model are needed to address any reduction in stiffness associated with discrete or highly localized slip events and cleavage fractures observed at larger indentation depths.

Some information contained in this report appears, in abbreviated form with far fewer figures, in a recently submitted publication (*37*).

5. References

1. Haussuhl, S. Elastic and Thermoelastic Properties of Selected Organic Crystals. *Zeit. fur Kristallographie* **2001**, 216, 339–353.

2. Haycraft, J.; Stevens, L.; Eckhardt, C. The Elastic Constants and Related Properties of the Energetic Material Cyclotrimethylene Trinitramine (RDX) Determined by Brillouin Scattering. *J. Chem. Phys.* **2006**, 124, 024712.

3. Ramos, K.; Hooks, D.; Bahr, D. Direct Observation of Plasticity and Quantitative Hardness Measurements in Single Crystal Cyclotrimethylene Trinitramine by Nanoindentation. *Philos. Mag.* **2009**, 89, 2381–2402.

4. Bowers, R.; Romans, J.; Zisman, W. Mechanisms Involved in Impact Sensitivity and Densensitization of RDX. *Ind. Eng. Chem. Prod. Res. Develop.* **1973**, 12, 2–13.

5. Kuklja, M.; Kunz, A. Compression-induced Effect on the Electronic Structure of Cyclotrimethylene Trinitramine Containing an Edge Dislocation. *J. Appl. Phys.* **2000**, 87, 2215–2218.

6. Hooks, D.; Ramos, K.; Martinez, A. Elastic-plastic Shock Wave Profiles in Oriented Single Crystals of Cyclotrimethylene Trinitramine (RDX) at 2.25 GPa. *J. Appl. Phys.* **2006**, 100, 024908.

7. Connick, W.; May, F. Dislocation Etching of Cyclotrimethylene Trinitramine Crystals. *J. Cryst. Growth* **1969**, 5, 65–69.

8. Halfpenny, P.; Roberts, K.; Sherwood, J. Dislocation Configurations in Single Crystals of Pentaerythritol Tetranitrate and Cyclotrimethylene Trinitramine. *J. Cryst. Growth* **1983**, 65, 524–529.

9. Elban, W.; Armstrong, R.; Yoo, K.; Rosemeier, R.; Yee, R. X-ray Reflection Topographic Study of Growth Defect and Microindentation Strain Fields in an RDX Explosive Crystal. *J. Mater. Sci.* **1989**, 24, 1273–1280.

10. Gallagher, H.; Halfpenny, P.; Miller, J.; Sherwood, J. Dislocation Slip Systems in Pentaerythritol Tetranitrate (PETN) and Cyclotrimethylene Trinitramine (RDX). *Phil. Trans. R. Soc. Lond. A* **1992**, 339, 293–303.

11. Ramos, K.; Bahr, D.; Hooks, D. Defect and Surface Asperity Dependent Yield During Contact Loading of an Organic Molecular Single Crystal. *Philos. Mag.* **2011**, 91, 1276–1285.

12. Cawkwell, M.; Ramos, K.; Hooks, D.; Sewell, T. Homogeneous Dislocation Nucleation in Cyclotrimethylene Trinitramine Under Shock Loading. *J. Appl. Phys.* **2010**, 107, 063512.

13. Cawkwell, M.; Sewell, T.; Zheng, L.; Thompson, D. Shock-induced Shear Bands in an Energetic Molecular Crystal: Application of Shock-front Absorbing Boundary Conditions to Molecular Dynamics Simulations. *Phys. Rev. B* **2008**, 78, 014107.

14. Ramos, K.; Hooks, D.; Sewell, T.; Cawkwell, M. Anomalous Hardening Under Shock Compression in (021)-oriented Cyclotrimethylene Trinitramine Single Crystals. *J. Appl. Phys.* **2010**, 108, 066105.

15. Miller, P. Effects of Pressure on the Thermal Decomposition Kinetics, Chemical Reactivity and Phase Behavior of RDX. *Combustion and Flame* **1991**, 83, 174–184.

16. Patterson, J.; Dreger, Z.; Gupta, Y. Shock-wave Induced Phase Transition in RDX Single Crystals. *J. Phys. Chem. B* **2007**, 111, 10897–10904.

17. Bedrov, D.; Hooper, J.; Smith, G.; Sewell, T. Shock-induced Transformations in Crystalline RDX: a Uniaxial Constant-stress Hugoniostat Molecular Dynamics Simulation Study. *J. Chem. Phys.* **2009**, 131, 034712.

18. Munday, L.; Chung, P.; Rice, B.; Solares, S. Simulations of High-pressure Phases in RDX. *J. Phys. Chem. B* **2011**, 115, 4378–4386.

19. Barton, N.; Winter, N.; Reaugh, J. Defect Evolution and Pore Collapse in Crystalline Energetic Materials. *Mod. Sim. Mater. Sci. Eng.* **2009**, 17, 035003.

20. Rimoli, J.; Gurses, E.; Ortiz, M. Shock-induced Subgrain Microstructures as Possible Homogeneous Sources of Hot Spots and Initiation Sites in Energetic Polycrystals. *Phys. Rev. B* **2010**, 81, 014112.

21. Winey, J.; Gupta, Y. Anisotropic Material Model and Wave Propagation Simulations for Shocked Pentaerythritol Tetranitrate Single Crystals. *J. Appl. Phys.* **2010**, 107, 103505.

22. Becker, R. Effects of Crystal Plasticity on Materials Loaded at High Pressures and Strain Rates. *Int. J. Plasticity* **2004**, 20, 1983–2006.

23. Olinger, B.; Roof, B.; Cady, H. The Linear and Volume Compression of β-HMX and RDX. In *Proc. Int. Symp. High Dynamic Pressures*; Commissariat a l'Energie Atomique: Paris, 1978; pp 3–8.

24. Clayton, J. *Nonlinear Mechanics of Crystals*; Springer: Dordrecht, 2011.

25. Cady, H. Coefficient of Thermal Expansion of Pentaerythritol Tetranitrate and Hexahydro-1,3,5-trinitro-s-triazine (RDX). *J. Chem. Eng. Data* **1972**, 17, 369–371.

26. Hill, R. The Elastic Behavior of a Crystalline Aggregate. *Proc. Phys. Soc. Lond. A* **1952**, 65, 349–354.

27. Schwarz, R.; Hooks, D.; Dick, J.; Archuleta, J.; Martinez, A. Resonant Ultrasound Spectroscopy Measurement of the Elastic Constants of Cyclotrimethylene Trinintramine. *J. Appl. Phys.* 98, 056106.

28. Sun, B.; Winey, J.; Hemmi, N.; Dreger, Z.; Zimmerman, K.; Gupta, Y.; Torchinsky, D.; Nelson, K. Second-order Elastic Constants of Pentaerythritol Tetranitrate and Cyclotrimethylene Trinitramine Using Impulsive Stimulated Thermal Scattering. *J. Appl. Phys.* **2008**, 104, 073517.

29. Sewell, T.; Bennett, C. Monte Carlo Calculations of the Elastic Moduli and Pressure-volume-temperature Equation of State for Hexahydro-1,3,5-trinitro-1,3,5-triazine. *J. Appl. Phys.* **2000**, 88, 88–95.

30. Zhao, J.; Winey, J.; Gupta, Y.; Perger, W. First-principles Studies of RDX Crystals Under Compression. In *Shock Compression of Compressed Matter*; Furnish, M., Elert, M., Russell, T., White, C., Eds.; AIP: 2006; pp 555–558.

31. McSkimin, H.; Andreatch, P.; Glynn, P. The Elastic Stiffness Moduli of Diamond. *J. Appl. Phys.* **1972**, 43, 985–987.

32. Herrero, C.; Ramirez, R. Structural and Thermodynamic Properties of Diamond: a Path-integral Monte Carlo Study. *Phys. Rev. B* **2000**, 63, 024103.

33. Nowak, R.; Manninen, T.; Heiskanen, K.; Sekino, T.; Hikasa, A.; Niihara, K.; Takagi, T. Peculiar Surface Deformation of Sapphire: Numerical Simulation of Nanoindentation. *Appl. Phys. Lett.* **2003**, 83, 5214–5216.

34. Timoshenko, S.; Goodier, J. *Theory of Elasticity*; third ed.; McGraw-Hill: New York, 1970.

35. Amuzu, J.; Briscoe, B.; Chaudhri, M. Frictional Properties of Explosives. *J. Phys. D: Appl. Phys.* **1976**, 9, 133–143.

36. Munday, L.; Chung, P.; Rice, B.; Solares, S. Phase Transition Behavior and Defect Structures of RDX Through Molecular Dynamics. In *Proc. 14th Int. Det. Symp.*; Coeur d'Alene, ID, 2010.

37. Clayton, J.; Becker, R. Elastic-plastic Behavior of RDX Single Crystals under Spherical Indentation: Modeling and Simulation. *J. Appl. Phys.* **2012**, , submitted.

Appendix. Rotated Elastic Constants

Let $\mathbb{C}^{(ijk)}$ be the fourth-order matrix of elastic constants of the crystal oriented for indentation into crystallographic plane (ijk). Let $\boldsymbol{R}^{(ijk)}$ be the corresponding rotation matrix. Then

$$\mathbb{C}^{(ijk)}_{ABCD} = R^{(ijk)}_{AE} R^{(ijk)}_{BF} R^{(ijk)}_{CG} R^{(ijk)}_{DH} \mathbb{C}_{EFGH}, \tag{A-1}$$

where $\mathbb{C}_{EFGH}$ corresponds to the isothermal elastic constants of table 2. Let $C^{(ijk)}_{\alpha\beta}$ denote the rotated elastic constants in Voigt's notation.

For indentation into (001) planes of RDX,

$$\boldsymbol{R}^{(ijk)} = [R^{(001)}_{AB}] = \begin{bmatrix} 1 & 0 & 0 \\ 0 & 1 & 0 \\ 0 & 0 & 1 \end{bmatrix}. \tag{A-2}$$

The second-order elastic constants of Haussuhl (*1*) are

$$\mathbb{C}^{(ijk)} = [C^{(001)}_{\alpha\beta}] = \begin{bmatrix} 24.56 & 7.61 & 5.30 & 0 & 0 & 0 \\ & 18.85 & 5.24 & 0 & 0 & 0 \\ & & 17.33 & 0 & 0 & 0 \\ & & & 5.15 & 0 & 0 \\ & \text{symm} & & & 4.06 & 0 \\ & & & & & 6.90 \end{bmatrix} \text{GPa}. \tag{A-3}$$

The second-order elastic constants of Haycraft et al. (*2*) are

$$\mathbb{C}^{(ijk)} = [C^{(001)}_{\alpha\beta}] = \begin{bmatrix} 36.48 & 0.90 & 1.26 & 0 & 0 & 0 \\ & 24.49 & 8.16 & 0 & 0 & 0 \\ & & 20.78 & 0 & 0 & 0 \\ & & & 11.99 & 0 & 0 \\ & \text{symm} & & & 2.72 & 0 \\ & & & & & 7.68 \end{bmatrix} \text{GPa}. \tag{A-4}$$

For indentation into (021) planes of RDX,

$$\boldsymbol{R}^{(ijk)} = [R_{AB}^{(021)}] = \begin{bmatrix} 1 & 0 & 0 \\ 0 & 0.475 & -0.880 \\ 0 & 0.880 & 0.475 \end{bmatrix}. \tag{A-5}$$

Rotated second-order elastic constants of Haussuhl (*1*) are

$$\mathbb{C}^{(ijk)} = [C_{\alpha\beta}^{(021)}] = \begin{bmatrix} 24.56 & 5.82 & 7.09 & 0.97 & 0 & 0 \\ & 16.78 & 6.13 & -0.27 & 0 & 0 \\ & & 17.62 & 0.90 & 0 & 0 \\ & & & 6.04 & 0 & 0 \\ & \text{symm} & & & 6.26 & 1.19 \\ & & & & & 4.70 \end{bmatrix} \text{GPa}. \tag{A-6}$$

Rotated second-order elastic constants of Haycraft et al. (*2*) are

$$\mathbb{C}^{(ijk)} = [C_{\alpha\beta}^{(021)}] = \begin{bmatrix} 36.48 & 1.18 & 0.98 & -0.15 & 0 & 0 \\ & 24.94 & 4.84 & 2.96 & 0 & 0 \\ & & 26.98 & -1.40 & 0 & 0 \\ & & & 8.67 & 0 & 0 \\ & \text{symm} & & & 6.56 & 2.07 \\ & & & & & 3.84 \end{bmatrix} \text{GPa}. \tag{A-7}$$

For indentation into (210) planes of RDX,

$$\boldsymbol{R}^{(ijk)} = [R_{AB}^{(210)}] = \begin{bmatrix} 0.495 & -0.869 & 0 \\ 0 & 0 & -1 \\ 0.869 & 0.495 & 0 \end{bmatrix}. \tag{A-8}$$

Rotated second-order elastic constants of Haussuhl (*1*) are

$$\mathbb{C}^{(ijk)} = [C_{\alpha\beta}^{(210)}] = \begin{bmatrix} 20.15 & 5.26 & 7.72 & 0 & 1.16 & 0 \\ & 17.33 & 5.29 & 0 & 0.03 & 0 \\ & & 23.06 & 0 & 1.29 & 0 \\ & & & 4.33 & 0 & -0.47 \\ & \text{symm} & & & 7.01 & 0 \\ & & & & & 4.88 \end{bmatrix} \text{GPa}. \tag{A-9}$$

Rotated second-order elastic constants of Haycraft et al. (*2*) are

$$\mathbb{C}^{(ijk)} = [C_{\alpha\beta}^{(210)}] = \begin{bmatrix} 22.17 & 6.47 & 6.16 & 0 & -0.54 & 0 \\ & 20.78 & 2.95 & 0 & -2.97 & 0 \\ & & 28.29 & 0 & 5.70 & 0 \\ & & & 4.99 & 0 & -3.99 \\ & \text{symm} & & & 12.94 & 0 \\ & & & & & 9.72 \end{bmatrix} \text{GPa.} \tag{A-10}$$

Perhaps most pertinent to indentation in the X_3-direction, $C_{33}^{(210)} > C_{33}^{(021)} > C_{33}^{(001)}$ for either set of experimentally measured elastic constants for RDX. It is also noted that $C_{33}^{(ijk)}$ from Brillouin scattering reported by Haycraft et al. (*2*) always exceeds the corresponding value from resonant ultrasonic measurements reported by Haussuhl (*1*).

Rotation matrices and elastic coefficients listed in equation A-2–A-10 are non-unique since additional rotation about the normal to plane (ijk) would not change the crystallographic plane normal to the direction of indentation. While some elastic constants would change under such additional rotation, the elastic constant $C_{33}^{(ijk)}$ would be unaffected. Furthermore, for spherical indentation into a cylindrical substrate, the total indentation force P would be unaffected by rigid rotation of the crystal lattice about X_3.

It is also illustrative to consider the elastic compliance matrix $\mathbb{S}$ obeying the reciprocity relations

$$\mathbb{S}_{ABEF}\mathbb{C}_{EFCD} = \frac{1}{2}(\delta_{AC}\delta_{BD} + \delta_{AD}\delta_{BC}). \tag{A-11}$$

Components of the 6×6 compliance tensor $S_{\alpha\beta}$ are those of the inverse of $C_{\alpha\beta}$. Young's moduli are defined as

$$E_{11} = 1/S_{11} = 1/\mathbb{S}_{1111}, \qquad E_{22} = 1/S_{22} = 1/\mathbb{S}_{2222}, \qquad E_{33} = 1/S_{33} = 1/\mathbb{S}_{3333}. \tag{A-12}$$

Values for Young's modulus for orientations corresponding to indentation on (001), (021), and (210) planes, with X_3 the direction of indentation, are listed in table A-1 for each set of elastic constants given in table 2.

Values of $E_{33}^{(ijk)}$ do not follow trends mentioned for those of $C_{33}^{(ijk)}$, and trends for Young's modulus also differ between different sets of experimentally measured constants. In particular, for elastic constants of Hausshul (*1*), $E_{33}^{(210)} > E_{33}^{(001)} > E_{33}^{(021)}$. For elastic constants of Haycraft

et al. (*2*), $E_{33}^{(021)} > E_{33}^{(210)} > E_{33}^{(001)}$. It is remarked that $E_{\alpha\alpha}^{(ijk)}$ from Haycraft et al. (*2*) always exceeds the corresponding value from Haussuhl (*1*) for $\alpha = 1,2,3$.

Table A-1. Young's modulus of RDX single crystals oriented for indentation on planes (001), (021), and (210).

	Plane [ref.(*1*)]			**Plane** [ref.(*2*)]		
Modulus	(001)	(021)	(210)	(001)	(021)	(210)
E_{11} [GPa]	20.85	20.85	16.72	36.40	36.40	19.12
E_{22} [GPa]	15.69	14.05	15.40	21.28	22.84	18.04
E_{33} [GPa]	15.40	14.19	19.31	18.04	25.55	23.61

NO. OF COPIES	ORGANIZATION
1 (PDF ONLY)	DEFENSE TECHNICAL INFORMATION CTR DTIC OCA 8725 JOHN J KINGMAN RD STE 0944 FORT BELVOIR VA 22060-6218
1	DIRECTOR US ARMY RESEARCH LAB IMNE ALC HRR 2800 POWDER MILL RD ADELPHI MD 20783-1197
1	DIRECTOR US ARMY RESEARCH LAB RDRL CIO LL 2800 POWDER MILL RD ADELPHI MD 20783-1197
1	DIRECTOR US ARMY RESEARCH LAB RDRL CIO MT 2800 POWDER MILL RD ADELPHI MD 20783-1197
1	DIRECTOR US ARMY RESEARCH LAB RDRL D 2800 POWDER MILL RD ADELPHI MD 20783-1197

NO. OF COPIES	ORGANIZATION
2	LOS ALAMOS NATL LABORATORY D HOOKS K RAMOS PO BOX 1663 LOS ALAMOS NM 87545
	ABERDEEN PROVING GROUND
49	DIR USARL RDRL CIH C P CHUNG J KNAP L MUNDAY RDRL WM B FORCH J MCCAULEY RDRL WML J NEWILL RDRL WML B I BATYREV J BRENNAN E BYRD S IZVYEKOV J MOORE R PESCE-RODRIGUEZ B RICE D TAYLOR N WEINGARTEN RDRL WML H B SCHUSTER RDRL WMM B G GAZONAS D HOPKINS RDRL WMP S SCHOENFELD RDRL WMP B R BECKER S BILYK D CASEM J CLAYTON (10 CPS) D DANDEKAR M GREENFIELD C HOPPEL R KRAFT B LEAVY D POWELL M RAFTENBERG S SATAPATHY M SCHEIDLER T WEERISOORIYA C WILLIAMS

NO. OF COPIES	ORGANIZATION
	RDRL WMP C T BJERKE S SEGLETES RDRL WMP F N GNIAZDOWSKI RDRL WMP G R EHLERS N ELDREDGE S KUKUCK